Periodicities in Solar Activity, Solar Radiation and Their Links with Terrestrial Environment

Valentina V. Zharkova[1,2*], Irina Vasilieva[2,3], Simon J. Shepherd[2,4], Elena Popova[5]

[1]Department of MPEE, University of Northumbria, Newcastle upon Tyne, UK; [2]ZVS Research Enterprise Ltd., London, UK; [3]Department of Solar Physics, Main Astronomical Observatory, Kyiv, Ukraine; [4]PRIMAL Research Group, Sorbonne Universite, Paris, France; [5]Centro de Investigación en Astronomía, Universidad Bernardo O'Higgins, Santiago, Chile

Correspondence to: Valentina V. Zharkova, *valja46@googlemail.com

ABSTRACT

Solar magnetic activity is expressed via variations of sunspots and active regions varying on different timescales. The most accepted is an 11-year period supposedly induced by the electromagnetic solar dynamo mechanism. There are also some shorter or longer timescales detected: the biennial cycle (2 - 2.7 years), Gleisberg cycle (80 - 100 years), and Hallstatt's cycle (2100 - 2300 years). Recently, using Principal Component Analysis (PCA) of the observed solar background magnetic field (SBMF), another period of 330 - 380 years, or Grand Solar Cycle (GSC), was derived from the summary curve of two eigenvectors of SBMF. In this paper, a spectral analysis of the averaged sunspot numbers, solar irradiance, and the summary curve of eigenvectors of SBMF was carried out using Morlet wavelet and Fourier transforms. We detect a 10.7-year cycle from the sunspots and modulus summary curve of eigenvectors as well a 22-year-cycle and the grand solar cycle of 342 - 350-years from the summary curve of eigenvectors. The Gleissberg centennial cycle is only detected on the full set of averaged sunspot numbers for 400 years or by adding a quadruple component to the summary curve of eigenvectors. Another period of 2200 - 2300 years is detected in the Holocene data of solar irradiance measured from the abundance of ^{14}C isotope. This period was also confirmed with the period of about 2000 - 2100 years derived from a baseline of the solar background magnetic field, supposedly, caused by the solar inertial motion (SIM) induced by the gravitation of large planets. The implication of these findings for different deposition of solar radiation into the northern and southern hemispheres of the Earth caused by the combined effects of the solar activity and solar inertial motion on the terrestrial atmosphere is also discussed.

1. INTRODUCTION

Currently, solar magnetic activity is expressed by the number of sunspots on the solar surface, by energetic events in the solar atmosphere, or by variations of various radioisotopes in the terrestrial biomass, which vary on a wide range of timescales. Most prominent is the 11-year solar cycle, which is significantly modulated by some longer timescales of a few hundred or a few thousand years. Solar activity is debated for decades to be linked to the variations of terrestrial temperature [1, 2] recently objected by IPCC. Understanding the nature of solar variability and the effects of the Sun on the terrestrial environment is the essential precondition for an attempt to predict future solar activity and terrestrial variation levels not only on 11 years but also on a longer timescale.

Furthermore, the frequencies derived from averaged sunspot numbers are shown by Cameron and Schussler, 2017 [3] to depend on the data they used: 1) sunspot data for the past 370 years and 2) the carbon isotope ^{14}C data 2 produced by a number of authors (see, for example [4, 5] and references therein). Data 1 does not contain any other data than those varying with 11-years period, as its size the full data 1 duration is within the size of a single grand solar cycle. The other frequencies of 93 and 200 years derived from sunspot index [3, 6] are assigned to the normal noise, although noting that these frequencies might be real. The carbon data 2 is strongly polluted by various other processes, e.g. a change of the local background intensity, natural conditions destroying the biomass, etc. that their conclusions should be taken with care [7].

Systematic properties of sunspot groups [8] indicate that they originate in the solar convection zone from a reservoir of the East-West orientated (toroidal) magnetic field. This magnetic field is generated by winding up a poloidal magnetic field (such as a dipole magnetic field aligned with the sun's rotation axis) by the differential rotation of the Sun so that its axisymmetric component dominates. The poloidal field is (re) generated against the effect of Ohmic decay by the collective effect of loops formed from the toroidal field by convective flows and/or magnetic buoyancy. The loops become twisted owing to the Coriolis force and thus acquire a systematic meridional component [9, 10]. This interaction of the toroidal and poloidal magnetic fields leads to a 22-year magnetic cycle and an 11-year cycle of sunspot activity [9, 10].

Jones *et al.*, 2010 [11] presented a detailed description of the four main models of the mean-field dynamo starting from the first one, Interface Dynamo, suggested by Parker (1955) [9], which was later modified by Parker (1993) [12] suggesting that the shear occurs in the tachocline and the α-effect in the convection zone. This separation is desirable because then the strong fields in the tachocline might not suppress the α-effect in the convection zone so much, and the tachocline is known to be the region of strong shear.

Second model, Flux Transport Dynamos, which goes back to the models of Babcock [10] and Leighton [13], is similar to the interface dynamo concept, in that they are α- dynamos, in which the shear is in the tachocline while the α-the effect is in the convection zone that can explain the observed twisting of a field in line with Joy's law. So far, this is quite similar to the interface dynamo, but the new feature of flux transport dynamos is that the poloidal flux is transported back to the tachocline by a meridional circulation rather than by diffusion alone [14, 15].

The third model, Tachocline Based Dynamos, has proposed, e.g. Spiegel [16] that the solar dynamo generation occurs in the tachocline and lower convection zone only. On this view, what one sees on the surface is merely a rather scrambled view of this process as the generated field rises through the convection zone to the surface. Low-order models demonstrate how nonlinear interactions can lead to the modulation of cyclic activity and solar luminosity.

These models may be constructed in two ways. The first involves the truncation of the relevant partial differential equations (in this case either the mean field equations or the full MHD equations). For nonlinear interactions of the magnetic field with the differential rotation, the dynamics reduces to a complex generalisation of the Lorenz equations [17]. If the magnetic field acts back on a dynamic alpha-effect then the structure of the low-order model is different [18].

An alternative way is to derive low-order models using normal-form theory and the underlying sym-

metries of the equations. This has the advantage that the dynamics found is structurally stable and robust (at least close to the initial bifurcation). Global Computational Models (see, for example [19, 20] are computational models, which are constructed to examine the generation of large-scale modes in a solar context. Computational models, though, have significant difficulty in reaching the correct parameter regime not only in the momentum equation but also for the induction equation itself.

There are also a number of papers describing the variability of solar activity with electromagnetic dynamo theory, which can be roughly divided into two classes: 1) nonlinear dynamics and deterministic chaos, and 2) random fluctuations of dynamo excitation. The nonlinear dynamics approach typically considers the bifurcation structure of low-order dynamical systems (see reviews [21, 22]) but models based on nonlinear turbulent PDEs have been also frequently investigated [23-26].

Hence, in general, dynamo theory produced by a dipole magnetic field is divided into two classes: large-scale and small-scale dynamo models [11, 27]. The authors [27] consider kinematic dynamo action in a sheared helical flow at moderate to high values of the magnetic Reynolds number (Rm). They find exponentially growing solutions that, for large enough shear, take the form of a coherent part embedded in incoherent fluctuations. They further argue that although the growth rate is determined by small-scale processes, the period of the coherent structures is set by mean-field considerations. It is obvious that some stochastic component in solar activity may possibly be present in the solar dynamo, as it is natural for large complex dynamical systems while a ratio between non-stochastic and stochastic components of solar activity are still debated depending on the model approaches.

Recently, Zharkova *et al.* [28, 29] suggested using an additional proxy of solar activity - the eigenvectors of the solar background (poloidal) magnetic field (SBMF), obtained from the low resolution synoptic magnetic maps of Wilcox Solar Observatory. These eigen vectors consider the low-magnitude solar background magnetic field and are not contaminated by strong magnetic fields of magnetic loops and sunspots [30], which are present in the high-resolution synoptic magnetic maps of Kitt Peak Observatory [31, 32]. By applying the principal component analysis (PCA) to the synoptic magnetic maps for cycles 21 - 23 [28] and, recently, for 21 - 24 [30] the authors identified and confirmed a number of eigenvalues and eigenvectors from the SBMF representing magnetic waves of the solar surface. The eigenvectors, or magnetic waves, are found to appear in pairs assumed to be generated by different magnetic sources in the solar interior, e.g. by a dipole, quadruple, sextuple sources, etc.

The first pair of eigenvectors covered by the largest amount of the magnetic data by variance, or principal components (PCs), reflects the primary waves generated by the solar dynamo produced by the dipole magnetic sources [29]. The temporal features of the summary curve of these two PCs show a remarkable resemblance to the sunspot index of solar activity (representing a toroidal magnetic field of active regions) for cycles 21 - 23 [29] and cycles 21 - 24 [30]. This correspondence occurs despite the PCs and sunspot indices representing very different entities of solar activity: poloidal magnetic field for PCs and toroidal magnetic field for sunspot numbers. However, their similarity and periodicity allowed too Zharkova *et al.* [29] to suggest using this summary curve of the two PCs of SBMF as a new, or additional, solar activity proxy.

The advantage of using the summary curve as a solar activity proxy instead of the averaged sunspot numbers is the use of the eigenvectors of the solar (poloidal) magnetic field oscillations, derived from the surface magnetic field measurements on the whole solar disk which are expressed then by mathematical formulae and, thus, can be extrapolated for any time. The ample magnetic full disk data significantly reduces the errors in the magnetic wave definition and introduces an extra-parameter, a leading polarity of SBMF [29], which is shown to be in anti-phase with the magnetic polarity of leading sunspots [33].

The two largest eigenvectors, or PCs, are the two different magnetic waves, which have amplitudes and phase shifts varying with time and latitudes. As a result, the summary curve of the resulting magnetic wave has some elements of stochasticity induced by the wave interference, caused by amplitude variations and the phase difference producing the envelope period of amplitude oscillation about 330 - 400 years called a grand solar cycle separated by grand solar minima [29, 34]. The phase shift between these two di-

pole waves changes the magnetic field shapes within 22-year cycles produced during grand solar cycles (GSC) [35]. The addition of the quadruple magnetic field can contribute to the formation of the centennial (Gleissberg) solar activity cycle [36] and can be directly linked to a flaring activity [30].

This new proxy of solar activity is essential progress in understanding the nature of solar activity because: 1) it considers directly a poloidal magnetic field used in dynamo models; 2) it derives that magnetic waves visible on the solar surface are the superposition of the waves created by dipole, quadruple, sextuple and octuple magnetic sources; 3) it detected that the dynamo waves are formed in pairs, or in two different layers, with the first pair data (67% by STD) linked to dipole magnetic sources; 4) superposition of these waves defines the observed magnetic waves on the solar surface.

Knowing this specific effect of the phase shifts, it makes much easier to model dynamo waves with similar phase shifts in each layer, whose superposition displays visible stochasticity without any heavy assumptions on other conditions in the solar interior as was required in other papers [3, 6] where stochastic dynamo equations were applied to two layers in the solar interior, instead of the normal mean dynamo models with meridional circulation.

Therefore, we need to clarify to what extent randomness, intrinsic periodicities apart from the 11-year cycle, and nonlinearities of the underlying dynamo process generating the solar magnetic field contribute to the observed long-term variability of solar activity. In fact, in the current paper, we will investigate the frequencies of solar activity derived from different datasets currently available. This analysis definitely indicates that the sunspot data has not only 11 but 22-year cycles. The latter makes much more sense, given the fact that the leading polarity change in sunspots is 22 years and not 11.

In addition, the analysis of variations of carbon ^{14}C isotope abundance [37] and irradiance oscillations over the past 12,000 years [38, 39] clearly demonstrate the well-defined millennial oscillations with a period of 2200 years [38, 40], 2300 years [41] or 2400 years [4]. These variations constitute the two-millennial Hallstatt's cycle of solar irradiance variations [41].

This Hallstatt cycle is also detected in the magnetic field baseline oscillations with the current Hallstatt's cycle to be started at the Maunder minimum and progress in ascending phase until 2500 - 2600 meaning the increase of solar irradiance during this period. Hence, this two-millennial period of solar irradiance oscillation combined with the grand solar cycle of 330 - 400 years, Gleisberg cycles of 80 - 100 years, and the basic cycles of solar activity of 11/22 years are the main ingredients of periodicities of solar activity we will attempt to consider in the current paper.

The overview of solar activity indices defined by sunspots is presented in Section 2, the recent restoration of the new solar activity index in a grand solar cycle is described in Section 3 while the two-millennial oscillations derived from oscillations of the solar irradiance and the baseline of eigenvectors of SBMF are described in Section 4 with the discussion and conclusions to be drawn in Section 5.

2. SPECTRAL ANALYSIS OF THE AVERAGED SUNSPOT NUMBERS

2.1. Wavelet and Fourier Spectral Analysis

The periods of oscillations can be derived from various datasets: averaged sunspot numbers, summary and modulus summary curves, solar irradiance, etc. using the spectral methods of Wavelet transform and Fourier analysis. Wavelet transform is a powerful tool to analyze time-series data collected by a pinpoint in the domain, to study the fluctuations in the frequency domain [42-44]. Wavelet analysis is often combined with Fourier analysis [44-47] to verify the wavelet findings.

Wavelet analysis is an excellent tool for examining signals with time-varying frequency characteristics. Unlike Fourier analysis [44-47], the wavelet transform gives a two-dimensional scan of the analyzed signal, while the time coordinate and frequency are independent variables. This representation allows you to explore the properties of signals simultaneously in time and frequency domains. The choice of the mother Morlet wavelet is dictated by the task to detect frequencies (or periods) and the nature of the signals under study because in the Morlet wavelet one can obtain a high-frequency resolution [43, 46], which is important for this task.

By considering the time series in the frequency-time space it is possible to derive dominant periods and their variations in time. Usually, the wavelet transform revealed richer features in the high-frequency region. For comparison in each wavelet panels we present the global wavelet spectra and the original Fourier spectra and Fourier spectra averaged by a period unit. The global wavelet spectrum is obtained by the integration of the coefficients of the wavelet transform over the time scale. The global wavelet spectra represent the distribution of temporal series over the duration-of-period axis and secure the noncontradictory estimations of power spectra of the series while reliably characterising temporal variations of the series.

To reflect the errors appearing during the wavelet analysis because of limited statistical data at the start and finish of the time series (border effects), the black dashed line marks the cone of influence (COI) defining the parts of the spectrum where these boarder effects become essential. For this reason the results outside the COI are excluded from further investigation. This is applicable, in particular, in calculations of the global wavelet spectrum. Global wavelet spectra are plotted by the black solid lines with COIs plotted by the black dashed lines, while the Fourier spectra are marked by indigo lines.

The significance level of the global wavelet spectrum is marked by the dashed red lines denoting the red noise spectra within the confidence interval of 95%. The peaks of the global wavelet spectra above the red noise with confidence level of 95% are considered to be significant.

2.2. Solar Activity Index by Averaged Sunspot Numbers

A system of the number of sunspots per day was introduced [48] by using the individual observations by preferred observers to compute, first, monthly averages, then yearly averages from the averages of all months, if in this year at least one observation is carried out. The very detailed sketches of the structure of sunspots were made by the observers with the quality not lower in detail than with modern telescopes.

A significant step in improving the sunspot series was made in 1998 by Hoyt and Schatten (HS) [49, 50] who published a revised sunspot series with sunspot groups (GSN) from 1610 based on the analysis of 455,242 records of 463 observers. HS98 used a special "fill-in" procedure to fill sunspot numbers for days with no observations, in order to "bridge" the data gaps.

A number of authors tried to understand the differences between the group numbers (GSN) and Wolf's sunspot numbers (WSN) [7, 51-53]. The GSN series of HS [50] is found to be more consistent and homogeneous with Schwabe's data throughout the entire studied period as found by [54] while the WSN records decreased by roughly 20% around 1848 because of the change of the primary observer from Schwabe to Wolf. Although, the GSN reconstruction becomes very similar to Wolf's reconstruction before the 1.25 correction factor was applied [51].

Clette *et al.* (2014) [52] reported a noticeable trend found and eliminated in the solar activity index derived from the observations of the Locarno Observatory, which was a reference observatory after 1980. Also the authors [52] derived the three-peak shape (so-called Ψ-type distribution) of the original GSN by HS [49, 50] for sunspot Cycle −1 with the peaks in 1736, 1739, and 1741. Later a modified single peak shape for this solar cycle was suggested by a number of authors (see, for example [55-58] after more historical records of sunspot counts were discovered. Although, the derivation by Clette *et al.* (2014) [52] indicated that the real shapes of cycles in early years were not yet confirmed.

Then an almost 400-year history of sunspot activity from 1610 to the 2000s was revised by joint efforts of researchers [59-61]. The project used the sketches of sunspots by Christoph Scheiner, Johann Kaspar Staudacher, Heinrich Schwabe, Rudolf Wolf, and Hisako Koyama [62, 63]. The authors used two backbones: the Schwabe (1794-1883) and the Wolfer (1841-1944) backbone [59].

Since July 2015, the SILSO International Data Center (Sunspot Index and Long-term Solar Observations) at the Royal Observatory of Belgium maintains a new, revised series of relative sunspot numbers SSN (Version 2.0), which was considered to be fairly reliable since 1750 [52, 54, 59]. This solar activity index SSN V2 will be used here for further analysis. The monthly smoothed sunspot numbers SSN version 2.0 [64] were used in this study as shown in **Figure 1**, top plot.
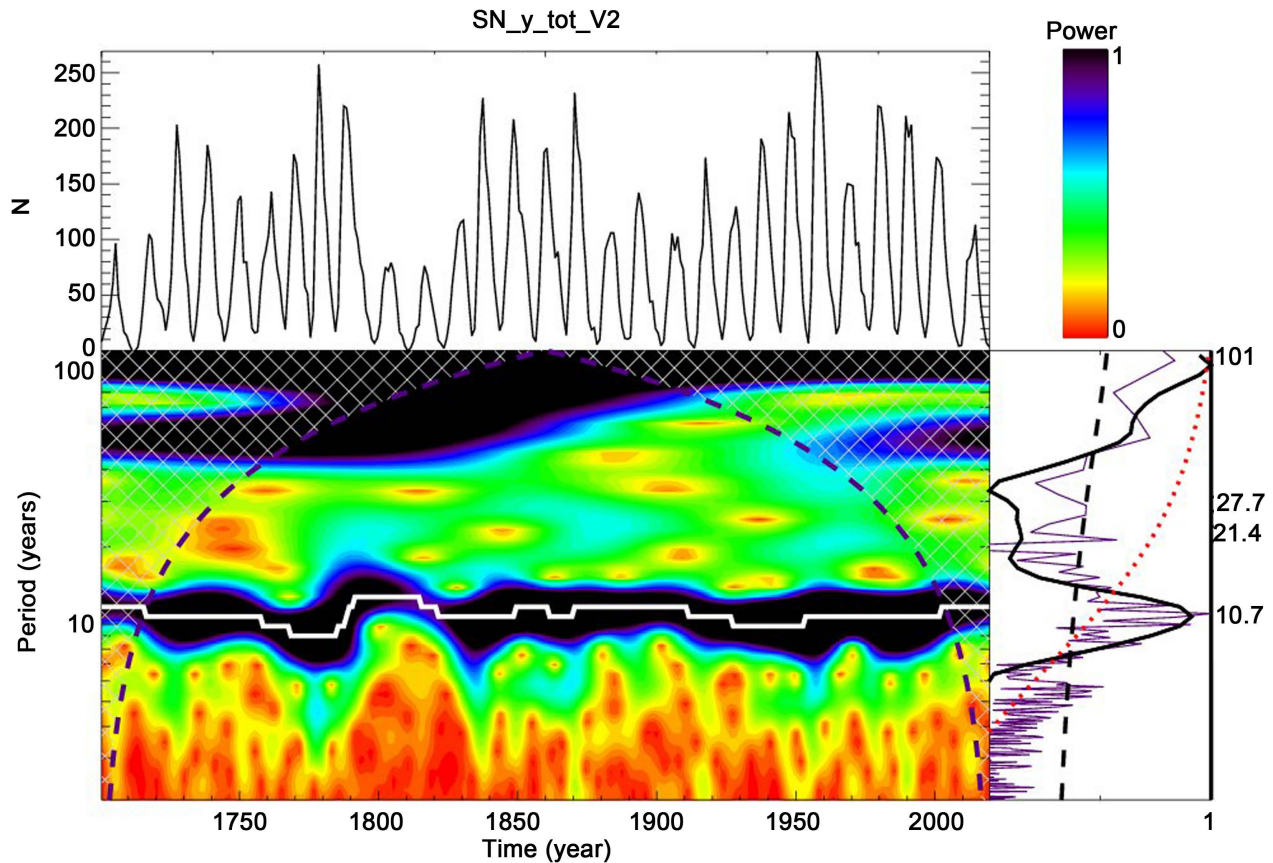
Figure 1. Top plots: Left - The averaged sunspot numbers *N* versus time in 1700-2020 including purely defined cycles. Right - The power bar for the wavelet spectrum. Bottom plots: Left - Wavelet spectrum with periods (Y-axis) derived from sunspot numbers, the black dashed line shows the Cone of Influence (COI) (see the text for details). Right - The global wavelet spectrum (the solid black line), its 95% confidence interval (black dashed line), the red-noise of the global wavelet spectrum at 95% confidence level (the red dashed line) (see for details Section 2.1). The Fourier spectrum is shown by the indigo line. The right Y-axis shows the derived periods in years. A courtesy of [35].

2.3. Periods Derived from the Averaged Sunspot Numbers

Now we wish to present periodicities embedded into the well-used averaged sunspot numbers observed in the past 400 years as derived earlier [35]. The Morlet wavelet analysis was applied to the frequencies of averaged sunspot number reported in Section 2 and the result is plotted Figure 1. The black solid line reflects the global wavelet spectrum, the black dashed line reflects the COI and the indigo line represents the Fourier spectrum. The red dashed line shows the red noise level of the data within the confidence interval of 95%. The peaks of the global wavelet spectra above the red noise with confidence level of 95% are considered to be significant.

The wavelet spectrum of the temporal series of averaged sunspot numbers for the whole series reveals the powerful peak at 10.7 years (corresponding to an 11-year cycle) and some smaller peaks at its double harmonics with a 21.4-year period. There are no other significant frequencies, or periods, detected besides a well-distinguished peak at 101 years, possibly, associated with Gleissberg's centennial cycle. This outcome is well expected since the sunspot data time limitations by default cannot carry any large-scale periods of higher frequencies because the dataset is rather short and contains only positive numbers of

sunspots with t considering the magnetic polarities of magnetic fields in them.

Although there is a weak flattening of the global wavelet spectrum at about 50 years period seen well below the red noise 95% confidence level. This peak is also supported by the weak peak in Fourier spectrum, which can be the indication of a real peak of solar activity reported for the sunspot diameters derived for cycles 12 - 24 [65]. However, this peak has no statistical significance yet in averaged sunspot numbers and its occurrence needs to be investigated further in the other proxies of solar activity discussed in the current paper.

This finding supports the objections expressed by the analysis of stochasticity of the averaged sunspot numbers [3] proving that 10.7 years is a real period of the oscillation of sunspot activity which can only reflect the positive variations of these sunspot numbers. In order to obtain other periods, we need to convert the data to the eigenvectors of SBMF which also include its polarity. The whole bulk of research discussed in the introduction was dedicated to the interpretation of this dataset and this period of dynamo wave generation.

3. SOLAR ACTIVITY INDEX BY EIGEN VECTORS OF SBMF

3.1. Pair of Principal Components and Their Summary Curve

The dynamo mechanism, which governs solar activity, operated with poloidal and toroidal magnetic fields [9], with the first one being the solar background magnetic field (SBMF), and the second one being the magnetic field of magnetic loops in active regions, which are embedded into the solar surface, whose roots are seen as sunspots. The interaction between these two magnetic fields defines the variations of solar activity seen through the appearance or disappearance of sunspots and active regions.

However, because the SBMF is shown to be in anti-phase with the leading polarity of a magnetic field in sunspots [33, 66] defining the locations and timing of sunspot appearances on the solar surface and their migration towards the solar equator or poles [33], one can expect that the summary curve of the SBMF should reveal defined links with the averaged sunspot numbers.

Zharkova and collaborators [28, 29, 67] investigated the two eigenvectors with the largest eigenvalues (39% by variance), or two principal components (PCs), or eigenvectors, of the solar background magnetic field (SBMF) by applying the principal component analysis (PCA) to the Wilcox Solar Observatory low-resolution full disk synoptic magnetic maps for cycles 21 - 24. The authors identified numerous eigenvalues and eigenvectors of own magnetic waves of the Sun seen on the solar surface, which came in pairs. The four significant pairs cover the majority (>95% of the data by variance [28, 30].

The first pair, or two principal components, reflect the primary waves of the solar magnetic dynamo produced by the dipole magnetic sources [29]. These two waves are found traveling slightly off-phase from one hemisphere to another and their interaction defines the solar activity in each hemisphere and as a whole [28]. Shepherd and Zharkova [29, 67] used the symbolic regression analysis [68] of these two magnetic waves and obtained the analytical expressions for the magnetic (dynamo) waves incorporated into the ensemble of waves present in the solar background magnetic field attributed to the poloidal field of the Sun [69]. These mathematical equations were used to make predictions in time by a thousand years both forwards and backwards, from the current epoch and to use them for a comparison with the magnetic waves supposedly produced by the solar dynamo acting in two layers with slightly different meridional circulation velocities [29].

In order to bring the detected trends in the SBMF closer to the currently-used index of solar activity, the averaged sunspot numbers, we calculated the summary component of the two PCs. The modulus summary curve was found to correlate closely with averaged sunspot numbers [29, 67]. Zharkova *et al.* (2015) [29] suggested using the summary curve of these two PCs as a new proxy of solar activity, instead of, or in addition to, the averaged sunspot numbers. This suggestion was confirmed by previous research with PCA of the solar magnetic synoptic maps of Kitt Peak observatory obtained with much higher resolution [30], which PCs, in fact, reflect the magnetic fields of active regions, e.g. toroidal magnetic field, well known to have the 11-year periodicity classified via averaged sunspot numbers. While in the lower resolu-

tion SBMF from WSO used in our previous research [28-30] the PCA detects the two PCs, or magnetic waves, of the poloidal magnetic field associated with dipole magnetic sources [29] and another three significant pairs associated with quadruple, sextuple and octuple magnetic sources [30].

Using the derived formulae, the summary curve was calculated backward to 1200 and forward to 3200 [29] as shown in **Figure 2**, top plot revealing very distinct variations of the cycle amplitudes in every 330-400 years, or grand solar cycles (GSCs). These grand solar cycles are separated by grand solar minima (GSMs), when the amplitudes of 11-year cycles become very small, similar to those reported in Maunder, Wolf and Oort and other grand solar minima [70, 71].

The timings of the grand solar minima are shown [29] to be defined by the interference of two magnetic dynamo waves generated in different layers with close but not equal frequencies defined by the different velocities of meridional circulation so-called beating effect). The calculation of the summary curve forward in time until 3200 has shown the further three grand solar cycles separated by the three GSMs with the first GSM1 to occur during the cycles 25 - 27, or in 2020-2053 [29]. During the modern GSM1, which already started, the maximum amplitudes of cycles will be smoothly decreasing to 80% of the cycle 24 amplitude in cycle 25, to just 30% of the cycle 24 maximum amplitude in cycle 26 and again to 70% of
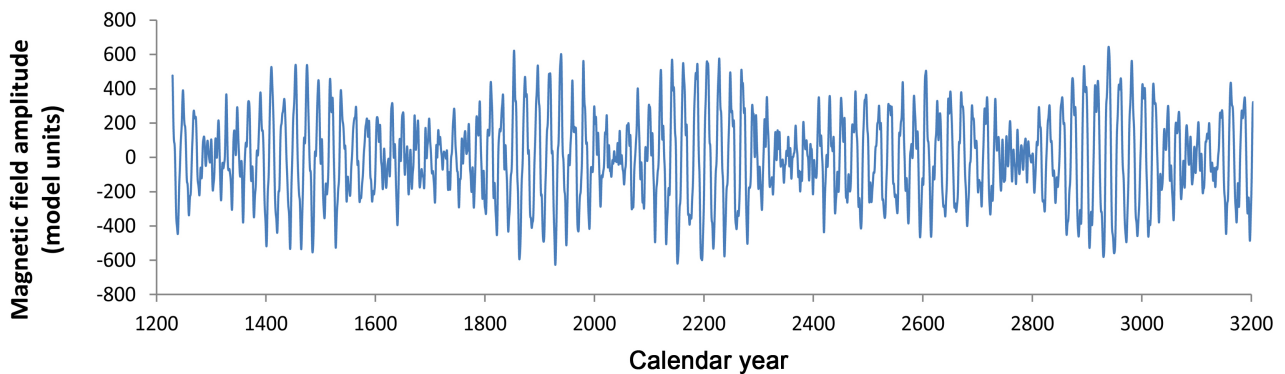
(a)
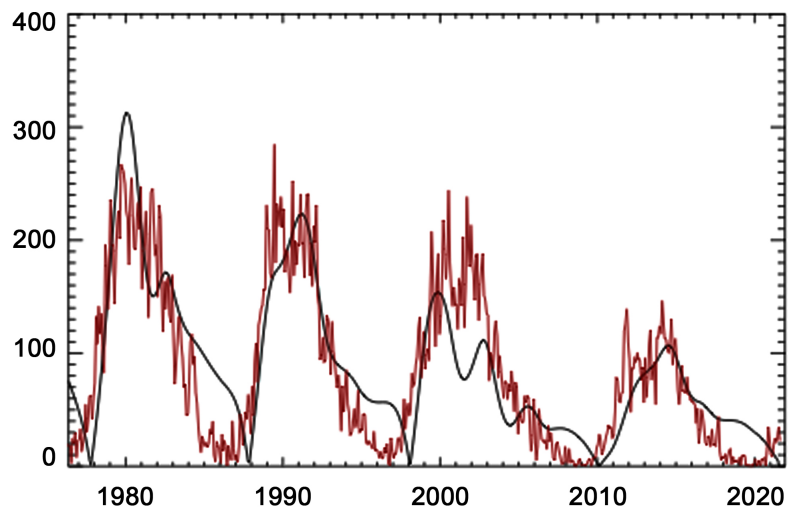
(b)

Figure 2. Top plot: The summary curve (Y-axis, arbitrary units) of two PCs calculated for 2000 years (a courtesy of [29, 34]). Bottom plot: the modulus summary curve (Y-axis, in arbitrary units) variations versus calendar years (X-axis) for solar cycles 21 - 24 (black line) compared with the averaged sunspot numbers (red line). A courtesy of [30].

cycle 24 amplitude in cycle 27. The next modern GSM2 will occur during four cycles in 2375 - 2415 [29, 34].

3.2. Modulus Summary Curve and the Sunspot Index

The modulus summary curve (MSC) reflecting the summary curve to the positive plane is shown in **Figure 2**, the bottom plot for cycles 21 - 24 [30]. The temporal features of a modulus of the summary curve of these two PCs show a remarkable resemblance to the sunspot index of solar activity for cycles 21 - 23 [29, 67], or recently cycles 21 - 24 [30].

Embracing the similarity between the modulus summary curve (MSC) and averaged sunspot numbers (SSN), the modulus summary curve can be normalised for each cycle by the averaged sunspot numbers indicated by the left Y-axis. The modulus curve, in general, follows the averaged sunspot numbers for all the cycles revealing a significant reduction of solar activity from cycle 21 (maximum about 300 sunspots), through cycle 22 (230), 23 (185) to cycle 24 (153) [30] that fits reasonably to the maximum numbers reported for cycles 21 - 24 [64]: 21 - 233, 22 - 213, 23 - 180, 24 - 150. The further predictions of the MSC reveal the continuing reduction of solar activity and the occurrence of grand solar minimum in cycles 25 - 27 [29].

There was a remarkable resemblance between these two curves, SSN and MSC shown in **Figure 2**, bottom plot taken from [29, 30, 35]. This similarity occurs despite the modulus summary curve reflecting the poloidal magnetic field while sunspots - toroidal one, which allowed the authors to suggest this summary curve of PCs, or eigenvectors of SBMF, as a new solar activity proxy. The advantages of using the solar index from the summary curve instead of the averaged sunspot numbers are the ability to do long-term predictions and the presence of the extra-parameter, a leading polarity of the background magnetic field of the Sun.

Hence, on the one hand, the modulus summary curve is found to be a good proxy of the traditional solar activity index contained in the averaged sunspot numbers predicting the grand solar minimum in the next three decades (2020-2053). This suggestion of reduced solar activity in cycles 25 - 27 was also supported by the recent research of the same SBMF data of WSO [72, 73] and by application to the series of sunspot numbers of the singular spectral analysis (SSA) [74] or Bayesian method [53]. At the same time, the summary curve proposed earlier [29, 67] as a sum of the largest eigenvectors of SBMF, which were given mathematical description via a series of cosine functions, is shown to represent a real physical process - poloidal field dynamo waves generated from dipole magnetic sources by the solar dynamo in two layers of the solar interior [29].

Therefore, the modulus summary curve proves that the eigenvectors of SBMF can be considered as a very good proxy of the traditional solar activity understandable by many observers. It should be used as a complementary solar activity index in addition to the existing one of the averaged sunspot numbers. Plus, this new index adds the additional parameter to this proxy of a dominant polarity of the solar background magnetic field for each cycle, which has the polarity opposite to the leading polarity of sunspots [33, 66].

Based on the similarity of the modulus summary and sunspot curves, one can conclude that the solar activity in cycles 21 - 24 is systematically decreasing with cycle number [29, 30] because of the shift in phase of the two magnetic waves so that their phase difference is increasing in time, approaching an anti-phase when there is a lack of any interaction between these two dynamo waves. This wave separation into the opposite phases will definitely lead to the absence of active regions, or magnetic flux tubes, whose roots appear on the solar surface as sunspots. This, in turn, can lead to an absence of noticeable activity on the solar surface, especially, in the descending and minimal phases of cycles 25 - 27 [29] that can resemble the similar features recorded during the Maunder Minimum [1].

3.3. Periods of Oscillation Derived from the Eigenvectors

### 3.3.1. Spectral Analysis of the Summary Curve

In order to extend the frequency detections, let us move to the dataset of eigenvectors derived as the summary curve of the two largest eigenvectors of the solar background magnetic field (poloidal field) [29].

We first analysed with the wavelet and Fourier transforms the shorter curve of 1200 years (2000 - 3200 (see **Figure 3**) and then the full curve of 2000 years (1200 - 3200) presented in our first paper [29] (see **Figure 4**). The results are shown with the original curve plotted in the top plots, **Figure 3** and **Figure 4**, the wavelet image shown in the bottom left plots and in the periods detected with the global wavelet and Fourier analysis, which are presented in the right plots.

It can be seen that for the summary curve of eigenvectors having as positive (northern polarity) so negative (southern polarity) magnitudes, none of the methods can detect any periodic oscillations except for 22 years (21.5 years, precisely) for the full set of the data (**Figure 4**). The same result with the most prominent cycle being about 21.4 years is achieved on a shorter timescale of the summary curve for 2200 - 3200 years shown in **Figure 3**. There is an indication in the Fourier spectrum of the detection of a larger cycle of 342 years in the short and 409 years in the full 2000 years of data. This indicates that, in order to detect the 11-year cycle, we need to convert the summary curve into a modulus summary curve and then repeat the analysis.

3.3.2. Spectral Analysis of the Modulus Summary Curve (MSC)

Now let us analyse with Morlet wavelet the modulus summary curves for these two summary curves
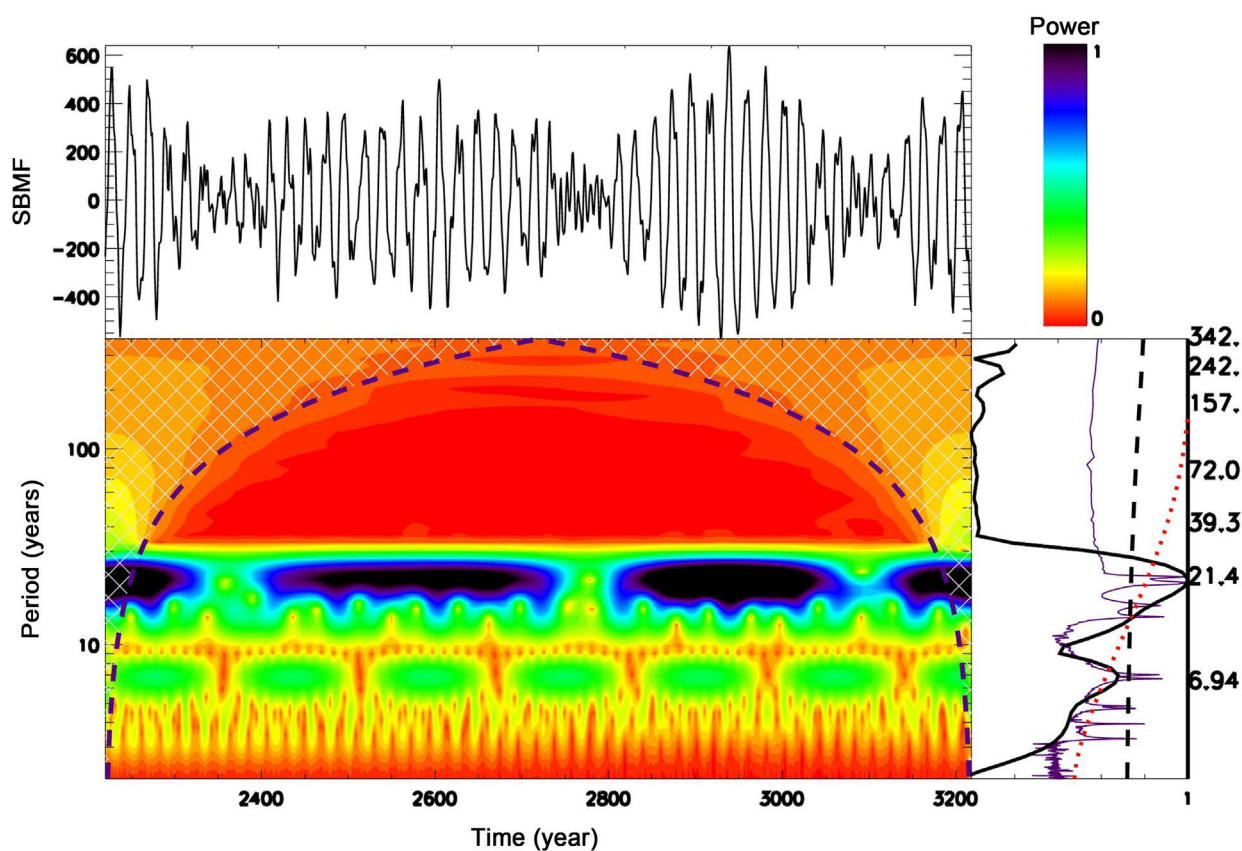
Figure 3. Left: Wavelet spectrum (bottom plot) with a power shown by the colour bar of the summary curve, E (Y-axis, in arbitrary units) (top plot) of the two largest eigenvectors of SBMF from Figure 2, the top plot for the years 2200 - 3200. Right: The global wavelet spectrum (the solid black line), its 95% confidence interval (the black dashed line), the red-noise of the global wavelet spectrum at 95% confidence level (the red dashed line). The Fourier spectrum is shown by the indigo line (see for details Section 2.1). The right Y-axis shows the derived periods in years. The period of 21.4 years is confidently located above the red noise level.
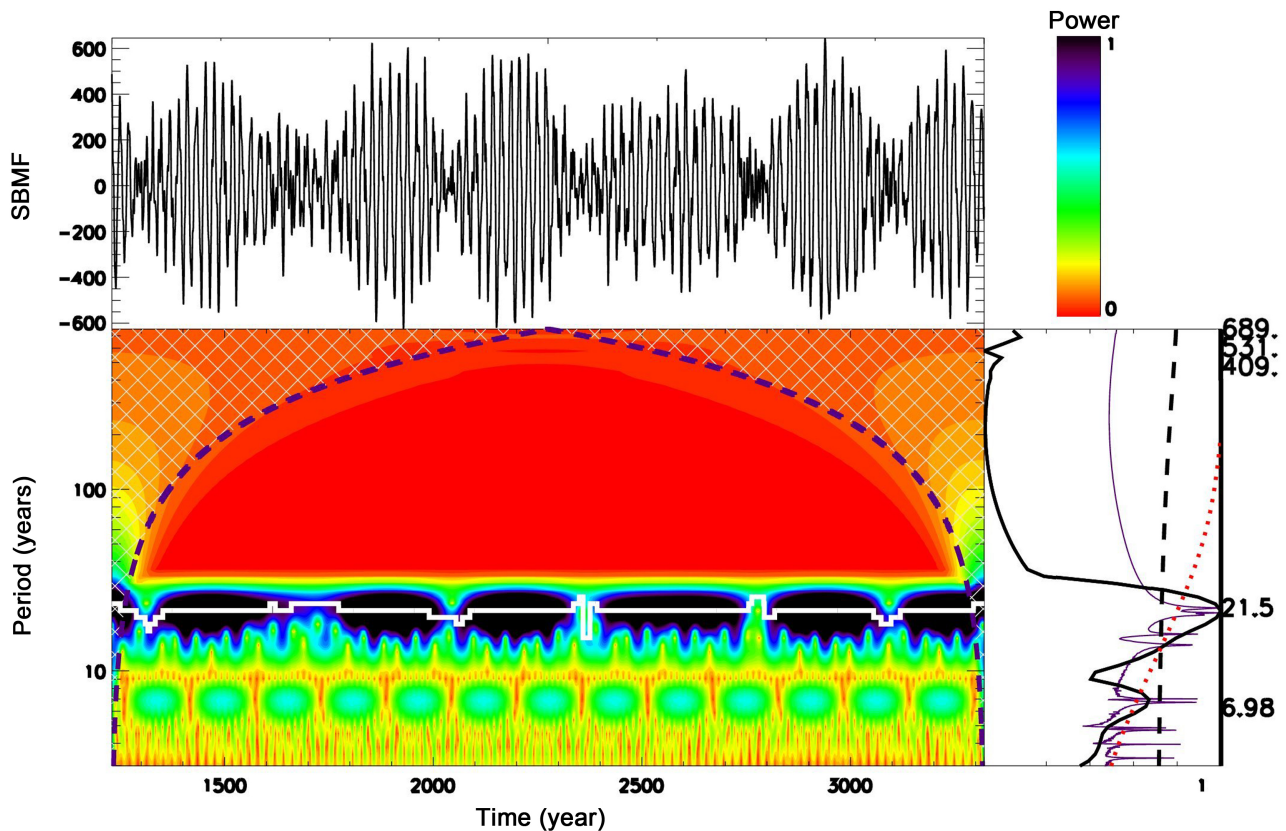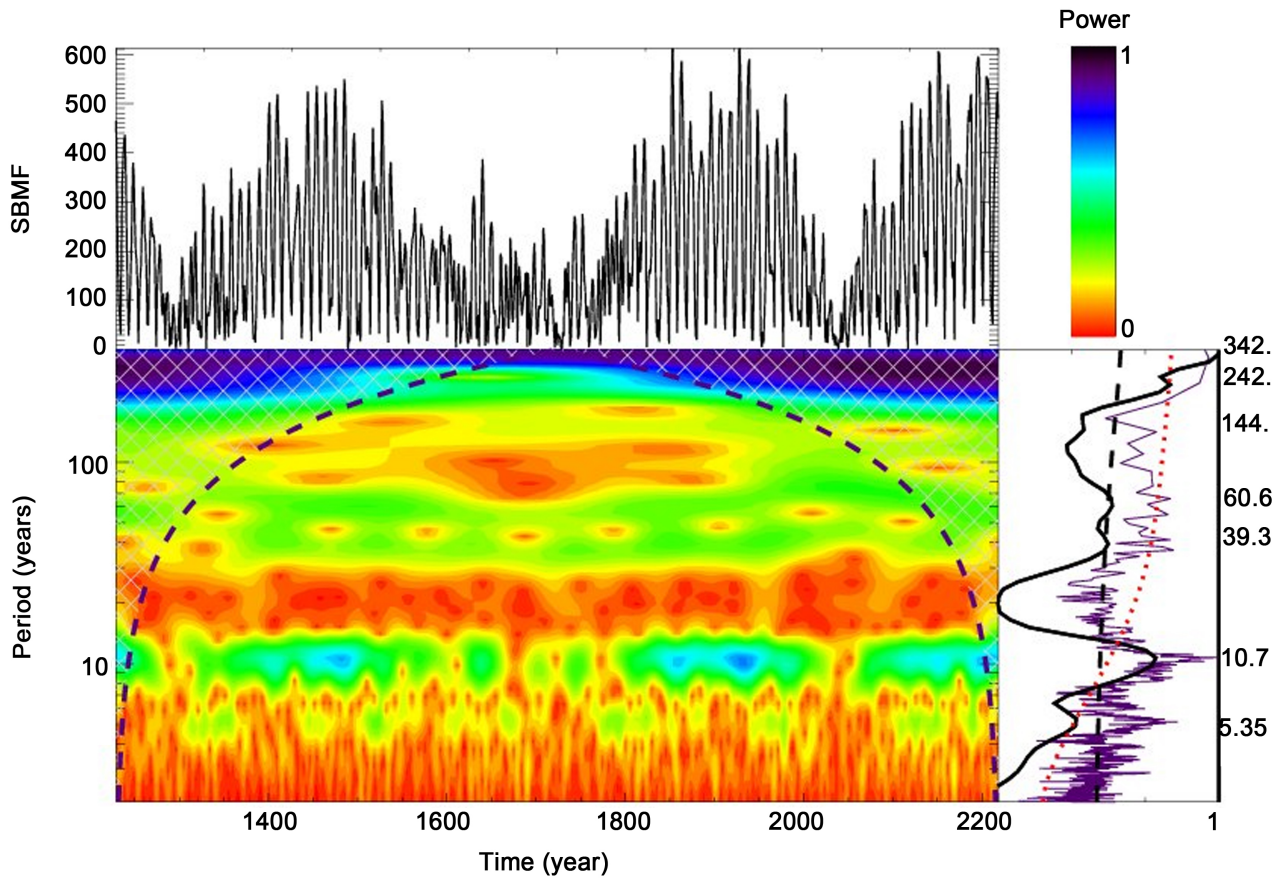
Figure 4. Left: Wavelet spectrum (bottom plot) with a power shown by the colour bar of the summary curve, E (Y-axis, in arbitrary units) (top plot) of the two largest eigenvectors of SBMF taken from Figure 2, top plot, for the years 1200 - 3200. Right: the global wavelet spectrum (the solid black line), its 95% confidence interval (the black dashed line), the red-noise of the global wavelet spectrum at 95% confidence level (the red dashed line). The Fourier spectrum is shown by the indigo line. For details see Section 2.1. The Y-axis shows the derived periods in years. The period of 21.5 years is confidently located above the red noise level.

of 1000 years (2200 - 3200) and of 2000 years (1200 - 3200) taken from our paper [29]. The results are shown in Figure 5 for the shorter period of 2200 - 3200 and in Figure 6 with the original curve plotted in the top plot, the wavelet analysis image in the bottom left plot and frequencies detected are presented in the bottom right plot confirmed with the Fourier spectrum.

The original modulus summary curves are plotted in the top plots, the wavelet spectrum in the bottom left plot, the color bar of the wavelet powers in the top right plot, and the global wavelet spectrum (solid black line) and Fourier spectrum (solid Indigo line) in the bottom right plot. The black dashed line in the wavelet and global wavelet spectrum marks the Cone of Influence (COI) defining the parts of the spectrum where the border effects of a wavelet analysis become essential and, thus, excluded from the further investigation.

The significance level of the global wavelet spectrum is marked in Figure 5, the right bottom image, by the dashed red lines denoting the red noise spectra within the confidence interval of 95%. Note that the power of the red noise grows with a reduction of frequency, e.g. with the growth of a period of oscillations. The peaks above the confidence level of 95% of the global wavelet spectra (dashed lines) are considered to be significant.

It can be seen that for the modulus summary curve of eigenvectors all having positive magnitudes, we
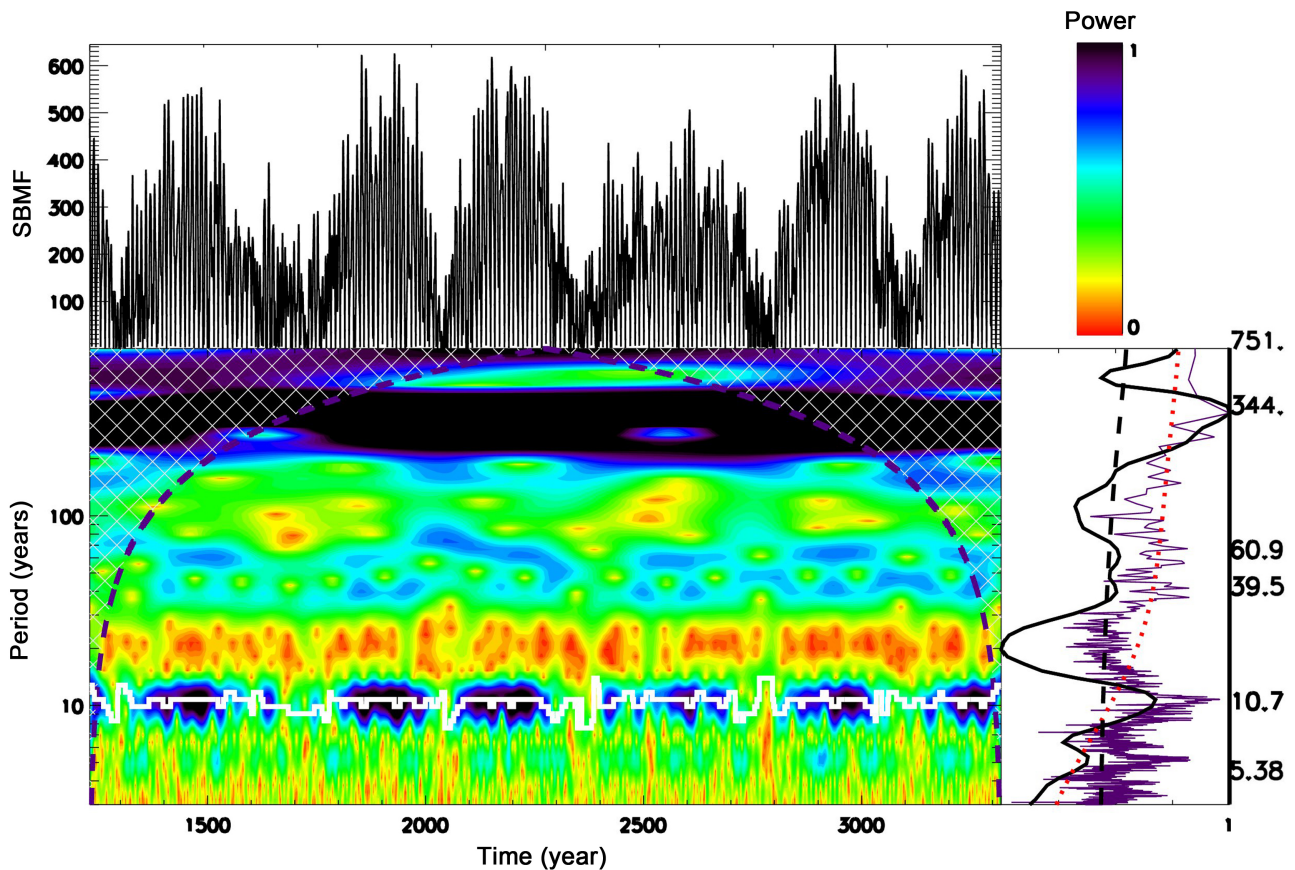
Figure 5. Left: Wavelet spectrum (with a power shown by the colour bar (bottom plot) of the modulus summary curve, E, (Y-axis in arbitrary units) (top plot) of the two largest eigenvectors of SBMF for the years 1200 - 2200 (X-axis). Right: The global wavelet spectrum (the solid black line), its 95% confidence interval (the black dashed line), the red-noise of the global wavelet spectrum at 95% confidence level (the red dashed line). The Fourier spectrum is shown by the indigo line (see for details Section 2.1). The right Y-axis shows the derived periods in years. A courtesy of [35].

detect the 11-year cycles (10.7 ± 1.4 years, precisely), similar to that derived from the sunspots. In addition, there are smaller maxima appearing on the harmonics of the 11-year cycle and a very strong maximum at 342 years for the shorted MSC and 344 years for the longer MSC of 2000 years. This corresponds to the averaged period of the grand solar cycle detected by Zharkova *et al.* (2015) [29] from the pair of eigenvectors derived from the SMBF.

Similar to the periods derived from the averaged sunspot numbers, there are two weak peaks of the global wavelet spectrum at about 39.3 and 60.6 year periods seen at the edge of 95% confidence interval well below the red noise 95% confidence level. These two peaks are also supported by the two peaks at the same periods in Fourier spectrum. This can be the further indication that the peaks of 44 years reported for the variations of sunspot diameters derived for cycles 12 - 24 [65] can be a real feature of magnetic flux tube variations and conditions of their appearance on the surface of the Sun as sunspots.

These weak peaks can appear as the interference of magnetic dynamo waves, similar to the period of 342 - 350 years produced by the interference (beating effect) of the two magnetic waves (principal components, or eigen vectors) produced by the solar dynamo in two layers with dipole magnetic sources [29] or the period of about 90 - 100 years produced by the interference of four waves, two from dipole and two from quadruple, magnetic sources [36]. Perhaps, the weaker periods can be reproduced by the further

Figure 6. Left: Wavelet spectrum (with a power shown by the color bar) (bottom plot) of the modulus summary curve E (Y-axis, in arbitrary units) (top plot) of the two largest eigenvectors of SBMF for the years 1200 - 2200. Right: The global wavelet spectrum (the black solid line), its 95% confidence level (the black dashed line), and the red noise of global wavelet spectrum at 95% confidence levels (the red dashed line), the Fourier spectrum (the indigo line) (see for details Section 2.1). The Y-axis shows the derived periods in years.

interference of the other four waves produced by sextuple and/or octuple magnetic sources [30]. Hence, the occurrence of these weak peaks and their validity needs to be investigated further.

A similar period of oscillation of 350 years, was also found from Fourier spectra of solar irradiance observed by two different observers [38, 40] (see **Figure 7**), it corresponds rather closely to the period of a grand solar cycle (GSC) found from the summary curve of eigenvectors of SBMF [29], which are shown to be generated by the interference of magnetic waves produced by dipole magnetic sources in two (inner and outer) layers of the solar interior.

3.4. Modelling Solar Activity with the Double Solar Dynamo Model

For the interpretation of the magnetic waves derived from the eigenvectors of SBMF, the Interface Dynamo models were considered for two layers at different depths, where the dynamo waves are generated by several (dipole [29] and quadruple [36]) magnetic sources. These models took into account meridional flows in two layers located at different depths (one close to the bottom of the convective zone and the other close to the solar surface [29]. The flows are assumed to have different velocities of meridional flows as shown in observations (see, for example [75] that consequently, leads to slightly different periods of the waves generated at different depths.
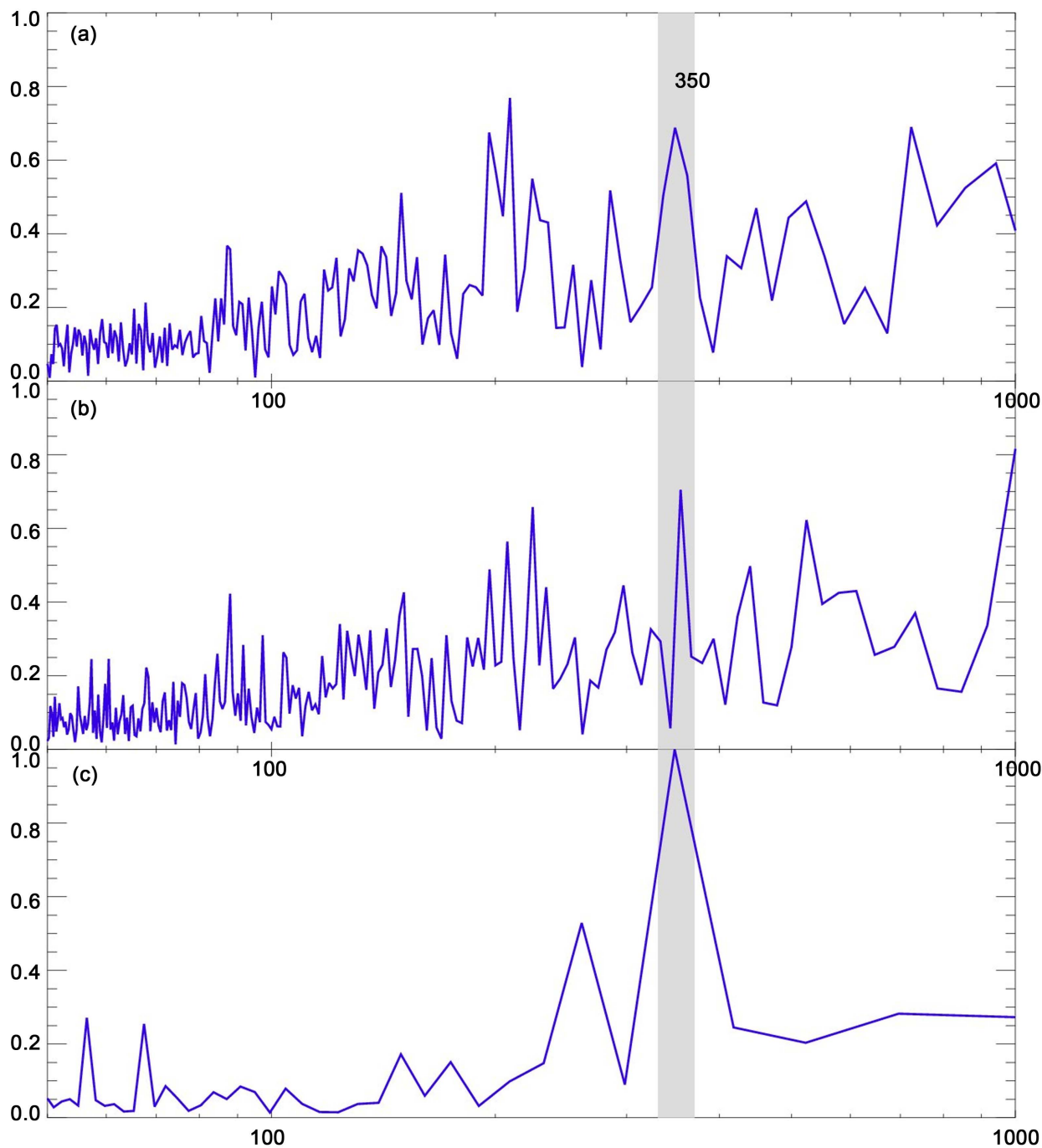
Figure 7. Comparison of Fourier spectra (Y-axis) of solar irradiance variations over the detected periods (X-axis) observed during the Holocene by Steinhilber *et al.* [40] (top plot), Vieira *et al.* [38] (middle plot) and derived from the modulus summary curve of SBMF (bottom plot) obtained from Figure 2, top plot, [29].

In the present work, we can use a low-mode approach for α-Ω dynamo with meridional circulation in two layers. For modelling a complex behavior of the magnetic field the low-mode approach was proposed and developed by a number of authors [36, 76-79] The main idea consists of the procedure where the system of differential equations, describing the magnetic field at the beginning of action is replaced by a dy-

namical system of not very high order equations selected in a certain way. In this case, we assume that one dynamo source is subsurface and another source is located deeply in the solar convection zone. The parameters that describe the magnetic field generation in each layer can be different, which can result in the simultaneous existence of two magnetic activity cycles with different periods.

The Parker dynamic equations [12], describing the generation and evolution of the solar magnetic field in a two-layer medium, are obtained from the system of electrodynamic equations for mean fields [80] on the assumption that the dynamo wave propagates in a thin spherical shell. In this case, the magnetic field is averaged along the radius within a certain spherical shell and the terms describing the curvature effects near the pole are deleted. In addition, in this approximation, we assume that the magnetic field is generated independently in either layer. Popova *et al*. (2008) [81] indicated how the meridional flows can be taken into account in the proposed dynamo model. As a result, the equations take the form:

$$\frac{\partial A_i}{\partial t} = R_{\alpha_i} \alpha_i B_i + \beta \frac{\partial^2 A_i}{\partial \theta^2} - V_i \frac{\partial A_i}{\partial \theta}, \tag{1}$$

$$\frac{\partial B_i}{\partial t} = R_{\omega_i} \sin\theta \frac{\partial A_i}{\partial \theta} + \beta \frac{\partial^2 B_i}{\partial \theta^2} - \frac{\partial V_i B_i}{\partial \theta}. \tag{2}$$

Here, B is the toroidal magnetic field, A is proportional to the toroidal component of the vector potential, which determines the poloidal magnetic field $B_P = -\frac{\partial A}{\partial \theta}$, and θ is the latitude measured from the pole. V_i is the meridional circulation (in terms of one degree per diffusion unit of time). Subscript i means the layer number (1 or 2). The factor $\sin\theta$ describes the decrease in the length of a line of latitude near the pole. The second equation neglects the small contribution of the α-effect, *i.e.* we use the so-called $\alpha\omega$ approximation. Curvature effects are absent in diffusion terms. It is assumed that the radial gradient of the angular velocity does not vary with θ. In the Equation (1) and Equation (2) the parameters R_α and R_ω describe intensity of the α-effect and the differential rotation, respectively, β is the coefficient of turbulent diffusion. We used a simple scheme for the stabilization of the magnetic field growth, namely, the algebraic quenching of the helicity. This scheme assumes that $\alpha = \alpha_0(\theta) / (1 + \xi^2 B^2) \approx \alpha_0(\theta)(1 - \xi^2 B^2)$, where $\alpha_0(\theta) = \cos\theta$ is the helicity in the unmagnetised medium and $B_0 = \xi^{-1}$ is the magnetic field for which the α-effect is considerably suppressed.

Proceeding from simple considerations, we can make certain assumptions concerning the circulation type (V_i). Since we consider a one-dimensional problem for either layer, we should consequently present the meridional circulation as a function only dependent on θ. If we assume that matter moving toward the poles leaves the layer where the dynamo operates, the meridional circulation vanishes at the poles and is maximal at mid-latitudes. We use $V_i = v_i \sin\theta$ as such a meridional circulation. To describe the poleward spread of matter in the upper layer and its return to the lower layer, it is necessary to specify the opposite signs to the meridional circulation in different layers. It was found that from helioseismological observations meridional circulation has two cells [75].

The basic idea of the low-mode approach is that the mean-field dynamo equations are projected onto a minimum set of several first eigenfunctions of the problem describing the decay of magnetic fields without any generation sources. In this case, it is necessary to choose the minimum set of functions in such a way that the solution, which is a set of several first time-dependent Fourier coefficients taking into account the generation sources, will describe the general behaviour of the magnetic field of a given object and will not describe this field with any lower set of functions. Substituting a chosen set of the components of a magnetic field into the dynamo equations one can obtain a dynamical system of equations containing the selected modes.

To study the behaviour of harmonics in our problem, consider the case $n = 10$, for which the dynamo number of the Sun is in the range of applicability of the method. We also took into account a larger number of harmonics and found that their contribution to the solution is negligible. The toroidal field B and the vector potential A can be represented as:

$$B(\theta,t) = \sum_{n=1}^{10} b_n(t)\sin(2n\theta) \qquad (3)$$

$$A(\theta,t) = \sum_{n=1}^{10} a_n(t)\sin((2n+1)\theta) \qquad (4)$$

Substituting the chosen type of solution into the System (1) and (2), we obtain a dynamic system of 20 equations for unknown functions $a_n(t)$ and $b_n(t)$. Since this system turns out to be too cumbersome, we do not present it here.

We have studied the behaviour of waves for dynamo numbers corresponding to solar plasma to be about −10,000. Calculations showed that the dependence of the cycle duration on the meridional circulation is almost linear, taking into account errors in normalisation. The temporal distributions of poloidal and toroidal magnetic fields produced by dipole magnetic sources are shown in **Figure 6** of the paper [29]. Here we present a comparison fit of the poloidal magnetic field derived from the dynamo model (**Figure 8**, bottom plot) to the summary curve derived from the eigenvectors of SBMF (**Figure 8**, top plot). It can
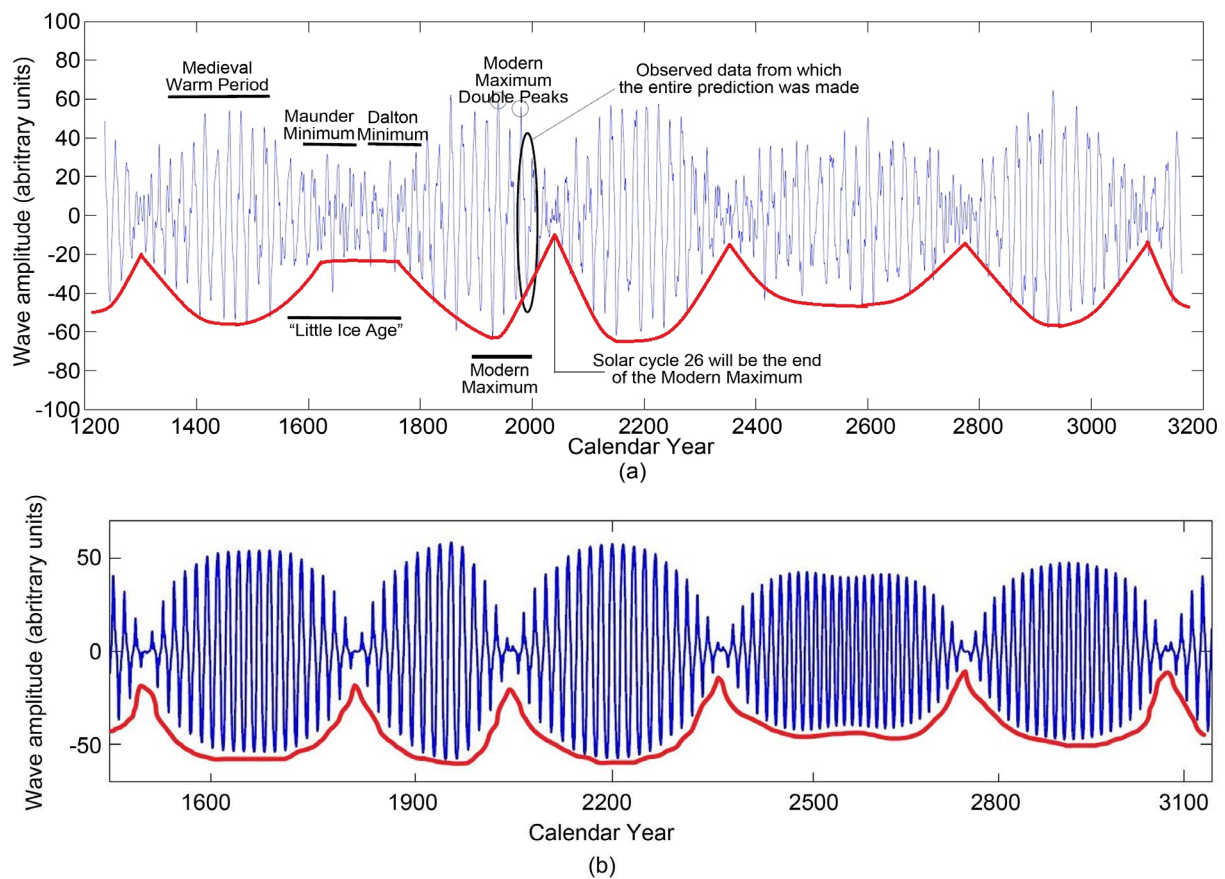
Figure 8. Top plot: The predicted summary wave (the sum of two principal components) (Y-axis, arbitrary units) calculated versus time (X-axis) from 1200 to 3200 years from the "historical" period (cycles 21 - 23) marked with a black oval (a courtesy of [29]). The historical maxima and minima of solar activity in the past are marked by horizontal brackets. Bottom plot: Variations of the summary poloidal magnetic fields (Y-axis, arbitrary unis) simulated for 2000 years with the two layers $\alpha\Omega$-dynamo model for dipole magnetic sources with the parameters derived from the two PCs. One arbitrary unit approximately corresponds to 1 - 1.5 Gauss. The red lines show the envelope curves reflecting the shape of the beating effect in amplitudes of the two-wave interference.

be noted that the simulated poloidal field variations fit rather closely the variations of amplitudes and cycle numbers in grand solar cycles derived from the eigen vectors as shown in **Figure 2**, top plot.

The interaction of the two dynamo waves generated at different depths of the solar interior, which have a phase shift increasing with time, leads to a beating effect in the amplitude with the overall period of 330 - 370 years, or the grand cycles, superimposed on a standard 22-year cycle [29]. These grand cycles are separated by Grand Solar Minima (GSMs) when the phase difference between the waves approaches nearly half of the period. Since the time in the dynamo models is normalised to the diffusion time, which depends on the coefficient of turbulent diffusion β in the medium, the meridional circulation velocities required to satisfy the observed grand solar cycles with the values of individual solar cycles (from 9 to 13 years) can be approximated by 9 and 10 m/s velocities in each layer for the cycle period of 11 years, in order to achieve the required beat of 340 - 380 years.

A grand solar cycle with the minima occurring every 330 - 380 years is likely to be a product of the beating effect of the two waves, which are generated in two different layers with slightly different meridional circulation velocities. Calculations have shown [29] that for a 22 years cycle of solar activity the beating effect between the waves generated in two layers can naturally occur if the meridional circulation velocities in these two layers are about 9 and 10 m/s, respectively. The beating effect between these waves with close periods of around 22 years can explain the variations of high-frequency amplitudes and the period of the low-frequency envelope wave with the period of 330 - 380 years in the resulting grand cycles seen in the observational curve (**Figure 2**, top plot).

The beauty of this low-mode double dynamo model shown here [29, 36] is that it fits the magnetic field waves derived from the eigenvectors of magnetic waves generated by dipole magnetic sources. Having two layers allows to reconcile the Interface Dynamo models valid in the bottom layer with turbulent dynamo models working in the shallow layer under the surface without changing dramatically the parameters of the solar plasma of both layers of the solar interior (dynamo numbers, α- and Ω parameters). This model allows us to obtain an elegant solution of dynamo equations for a very reasonable difference in the velocities of meridional circulation in these two layers not exceeding 1 m/s.

Furthermore, Popova *et al.* (2018) [36] added the effect of additional magnetic waves generated by quadruple magnetic sources in these layers that allowed them to simulate the centennial (Gleissberg) cycle. Using the dynamo model with meridional circulation and selecting the directions of circulation for quadruple waves, the authors estimate the parameters of quadruple waves best fitting the observations in the past grand cycle.

The comparison shows that the quadruple wave has to be generated in the inner layer of the solar convective zone, in order to provide the additional minima observed in the 19th and 20th centuries, thus, naturally accounting for the Gleissberg's centennial cycle. The resulting curve comprised from the summary curve for dipole magnetic sources and the simulated dynamo waves for quadruple sources reveals much closer correspondence to the averaged sunspot numbers derived in the current grand cycle. By considering the interference of two dipole and one quadruple waves, the paper by Popova *et al.* (2018) [36] reproduces the revised summary curve for the last 400 years which is able to account for the additional minima of solar activity, which occurred at the beginning of the 19th (Dalton minimum) and 20th centuries.

Another period not discussed here is the quasi-biennial period of about 2 - 2.7 years reported from different magnetic field observations [33, 82]. The appearance of the quasi-biennial cycles in the observations was shown to be reproduced with a contribution of the transport dynamo, in which the meridional circulation participates in the generation of the magnetic field, transfers it, and acts to shorten the cycle periods [79].

4. TWO-MILLENNIAL PERIODS IN VARIATIONS OF THE SOLAR IRRADIANCE AND SBMF BASELINE

4.1. Periods Detected in Oscillations of Solar Irradiance

There is also a two-millennial period recorded in the variations of solar radiation recorded from the

terrestrial biomass with the abundances of isotopes of carbon ^{14}C and beryllium ^{10}Be [38-40]. The variations over the past 12,000 years of the carbon ^{14}C isotope abundance are plotted in **Figure 9** (top plot) [37] and the derived solar irradiance oscillations [38, 39] are shown in **Figure 9** (bottom plot).

Let us now apply the Morlet wavelet and Fourier analysis to the solar irradiance data. In **Figure 10** we present 10,000 years of the solar irradiance (top left plot) gathered from the abundances of carbon 14 isotope in the terrestrial biomass derived by Steinhilber *et al.* (2012) [40], the Morlet wavelet in the bottom


(a)
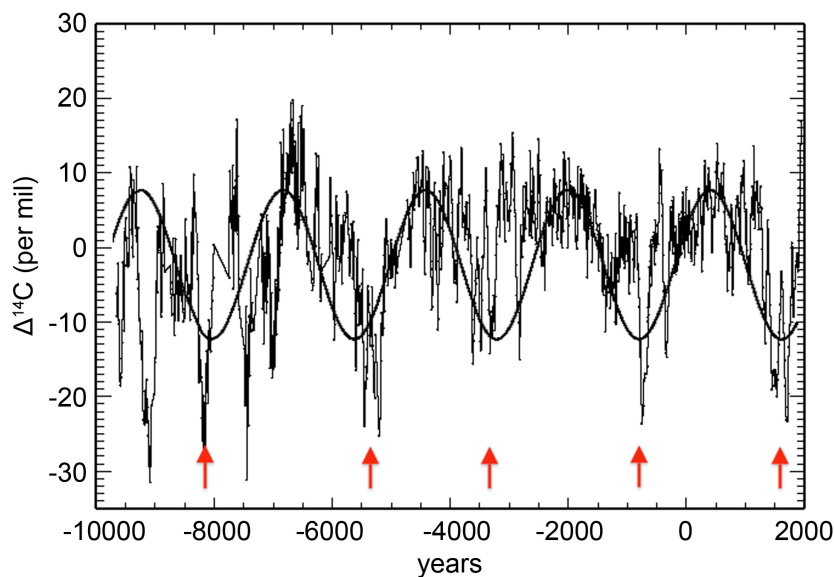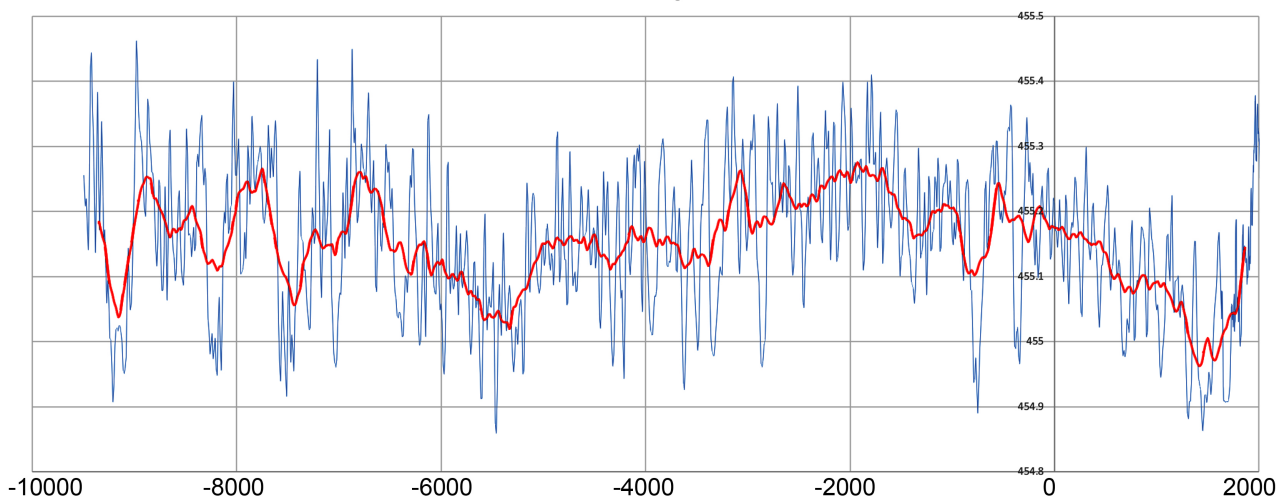
(b)

Figure 9. *Top plot*: the oscillations of the carbon ^{14}C isotope abundances from [37] for solar irradiance dating in the IntCal09 data, which also reveal the Hallstatt cycle period (about 2200 years). *Bottom plot*: the unnormalised solar irradiance (Y-axis) recovered for the holocene [83, 38] versus calendar years (X-axis), which demonstrates weak oscillations in the filtered (red) line with a period of about 2200 - 2300 years, similar to those reported in our unfairly retracted paper [84] and confirmed later with the real Sun-Earth ephemeris [85].

left plot and the Fourier spectrum derived from this solar irradiance curve. It can be seen that the wavelet transform provides a rather confident wide peak at about 2000 - 2300 years (the wide navy blue strip in the wavelet spectrum top) [40] coinciding with a sharp peak at 2243 years given by the global wavelet and Fourier spectra. Although red noise errors in the wavelet spectra become very high as shown by the reed dashed line. The Fourier spectrum thought detects this two millennium peak together with some smaller peaks between 216, 363, and 471 years, which probably can account for the grand solar cycles reported in Section 3.

It should be noted that the amount of ^{14}C and ^{10}Be on Earth depend not only on solar activity but on many terrestrial reasons including the variations in intensity of the Earth's magnetic field (see for example [4, 5]). However, the evolution of the geometry of this field in the past is not known and cannot be confidently included [86]. This definitely can increase errors for any periods defined with wavelet spectral analysis, and in particular, the exact number for the two-millennium period found in the wavelet spectrum. The validity of this two-millennial period is confirmed by the COI and the red noise errors at 95% confidence level as shown in Figure 10, although the exact numbers of this period can vary. This is why the further verification of detected wavelet periods was carried out with Fourier analysis.

The wavelet analysis was applied to the observations of solar irradiance observed in from 9000BC to 2000AD by Vieira *et al.* (2011) citevieira2011 and the result of wavelet and Fourier spectra are shown in Figure 11. It can be seen that the wavelet transform provides a wide peak at about 2100 - 2400 years while
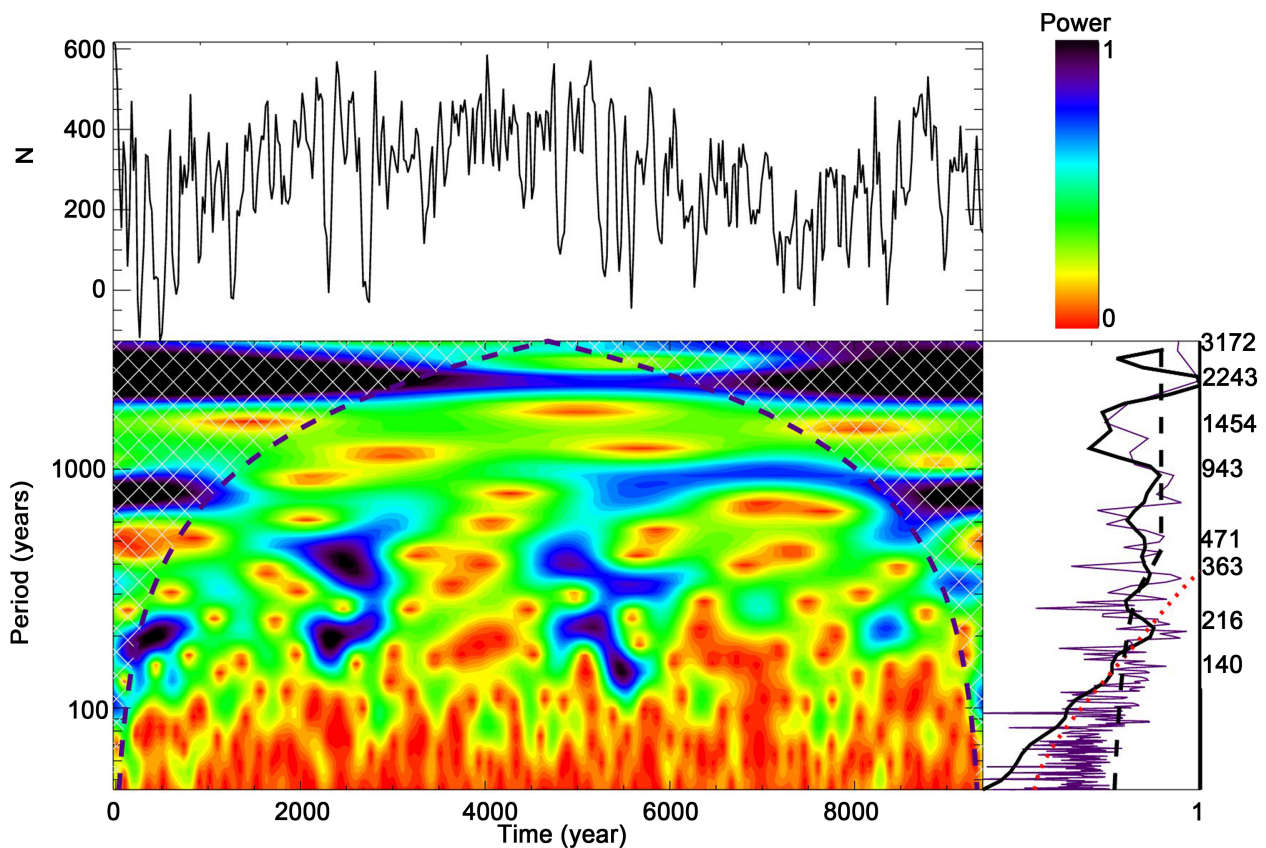
Figure 10. Left: Wavelet spectrum (bottom plot) with a power shown by the colour bar of the total solar irradiance, N, derived for the Holocene by [40] (top plot). Right: Global wavelet spectrum is plotted by the black solid line, the COI by the black dashed line, Fourier spectrum is marked by the indigo line and the red noise at 95% confidence level is shown by the red line (see for details Section 2.1). The Y-axis shows the derived periods in years.
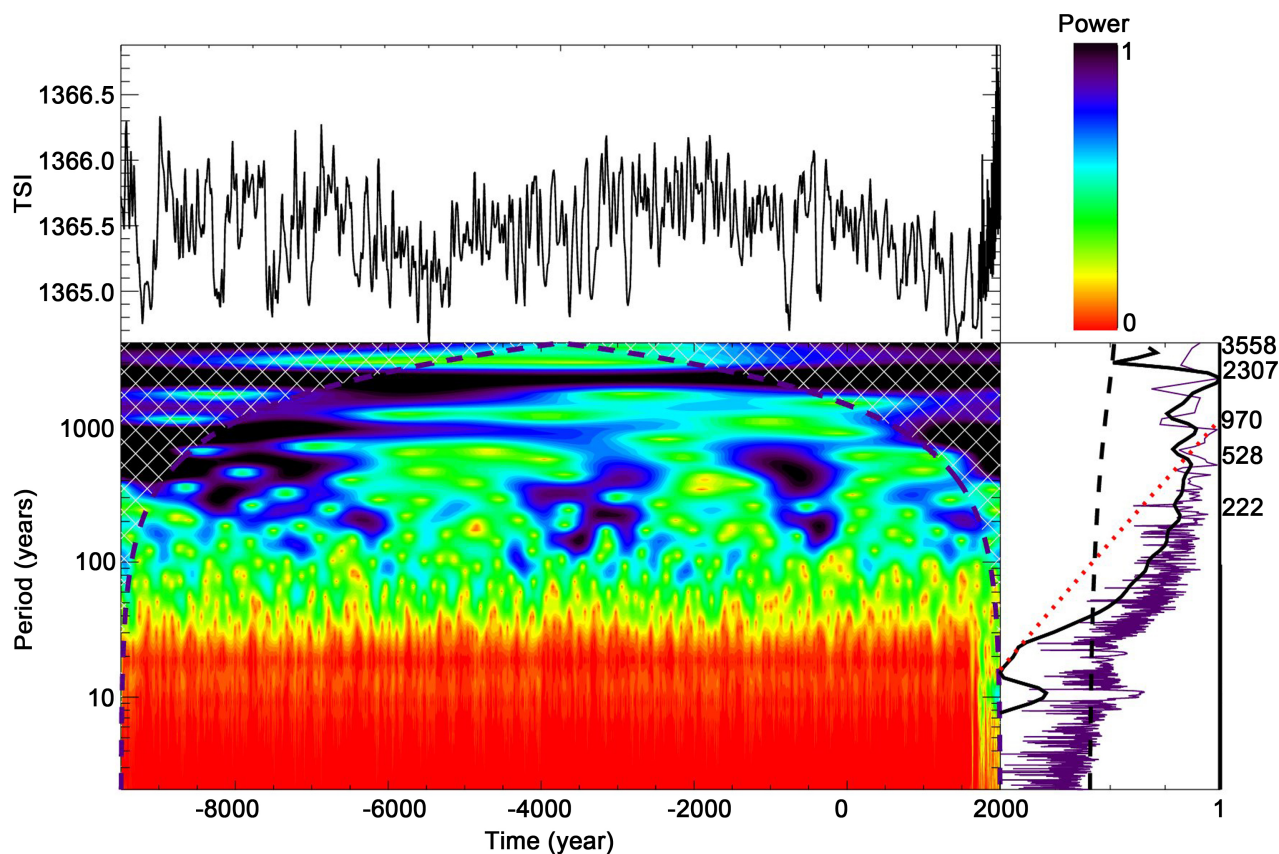
Figure 11. Left: Wavelet spectrum (bottom plot) with a power shown by the color bar of the total solar irradiance, N, derived for the Holocene by [38] (top plot). Right: Global wavelet spectrum is plotted by the black solid line, the COI by the black dashed line, Fourier spectrum is marked by the indigo line and the red noise at 95% confidence level is shown by the red line (see for details Section 2.1). The Y-axis shows the derived periods in years.

the global wavelet and Fourier spectra give the sharp peak at 2307 years. The red noise level for this dataset is much lower than that of [40] being below 95% confidence level. The Fourier spectrum also managed to detect a standard 11-year cycle peak at 10.7 years and some peaks associated with the grand solar cycle between 222, 374, and 528 years. This baseline oscillation period of 2100 years is very close to the periods of 2200 - 2400 years called Hallstatt cycle reported from the other observations of the Sun and planets [4, 40, 83, 87-89].

The full Fourier spectra of the solar irradiance curves by [40] and by [38] reveal a well-detectable peak at 350 years shown in Figure 7 (top plot). The nature of a grand solar cycle can be assigned to the beating effects of two dynamo waves formed in two different (inner and outer) layers of the solar interior by dipole magnetic sources as discussed in Section 3. The proposed nature of the two-millennia (Hallstatt) cycles detected in solar irradiance is discussed in the sections below.

There was another dataset of the oscillations of solar irradiance derived from the terrestrial biomass, whose analysis with the wavelet transform and singular spectral analysis (SSA) produced the two-millennial period of 2400 years by Usooskin *et al.* (2016) [4]. This data could not be accessed, so we evaluated the published plots. The evaluation has found the following problems:

1) The wavelet spectrum shown in their Figure 7 [4] reveals very patched wavelet powers that is clearly seen in the coloured patterns unlike the other two TSI dataset analysed in the current paper (see Figure 10 and Figure 11). The two millennial periods in the two datasets presented by navy blue patterns

in our wavelets are smooth and narrow while the terracotta patterns presented by Usoskin *et al.* (2016) [4] are extremely wide and have a break between −4000 and −3000 years.

2) The mean period derived from the wavelet power in [4] looks more likely to range between 2048 and 2500 years. However, without a global wavelet spectrum it is difficult to define more precisely the period magnitude.

3) The authors do not provide the Cone of Influence (COI) of their data.

4) There is no estimation of the red noise of the dataset.

5) Given the very patchy wavelet powers shown in Figure 7 [4], the red noise of this particular dataset could be substantial. This noise would significantly affect the period derived from it with the wavelet and SSA methods producing the number of 2400 years versus to the numbers 2243 years [40], 2305 years [38].

Which of the periods is more precise, it is rather difficult to say, given the complexity of building these databases from the terrestrial biomass [7] that would require further investigation.

### Looking for Reasons: Oscillations of the Baseline of SBMF

The large two-millennial period of oscillation of solar irradiance, Halllstatt's cycle, has been also detected from the summary curve of the eigenvectors [84, 85]. Note that the paper [84] was retracted by the Editor on the basis that the Sun-Earth distances cannot change on the large scale as the authors suggested. Later the book chapter by Zharkova (2021) [85] has shown from the official Sun-Earth distance ephemeris that the retraction basis was wrong, because the Sun-Earth distances indeed are changing significantly in the current millennium (1600 - 2600) compared to the previous one (600 - 1600). The chapter by Zharkova (2021) [85] proved that the paper by Zharkova *et al.* (2019) [84] was unfairly retracted.

To demonstrate the signs of two millennial cycle in the solar magnetic field, in Figure 12 we present 12,000 years of the summary curve (between the years of 10000BC and 2020AD [84, 85]. It shows that, in addition to the grand cycles of solar activity of 350 - 400 years, there are also indications of the clustered five grand solar cycles (GSCs), which are marked by the vertical lines separating larger cycles, or super-grand cycles of about two thousand years (Figure 12 top plot). By comparing the semi-similar features (between the vertical lines) of the repeated six grand cycles with a total duration of about 2100 years, one can see a striking similarity of the shapes of these grand cycles in each section. It can be also noted from the irradiance curve seen in both plots of Figure 10 that the new two-millennial cycle was likely to start 350 - 370 years ago, during the Maunder minimum [84, 85], and the solar irradiance is currently increasing as the observations show [40].

In order to understand the nature of these super-grand oscillations of TSI and to derive the exact frequency/period of this super-grand cycle, let us filter out large oscillations of 11/22 year solar cycles in the summary curve of two eigenvectors of SBMF by deriving the residual of the 22-year cycle amplitude, or a baseline magnetic field for the 22-year cycle. Theoretically, this should be a zero-line, a straight line with a zero magnitude of a magnetic field, while, in reality, the derived baseline shows the oscillations about this zero-line plotted by a dark blue curve in Figure 12 (bottom plot) over-plotted on the summary curve itself (light blue curve) taken from the summary curve calculated backward by 20 thousand years. The left Y-axis gives the range of variations of the baseline curve (−20, 20) while the right side Y-axis produces the range for the summary curve (−500, 500).

It is evident that the dark blue line in Figure 12 (bottom plot) shows much (≈25 times) smaller oscillations of the baseline of the magnetic field with a period of $T_{SG} = 2000 \pm 95$ years, which is incorporated into the magnetic field measurements of the summary curve (light blue curve). The baseline oscillations show a very stable period occurring during the whole duration of the simulations of 120 thousand years, for which the summary curve was calculated. This means that this oscillation of the baseline magnetic field on a millennial timescale has to be induced by a rather stable process either inside or outside the Sun.

This baseline oscillation period of 2100 years is very close to the 2200 - 2400 years period called Hallstatt's cycle reported from other observations of the total solar irradiance and planets [4, 40, 83, 87-89].

(a)

(b)
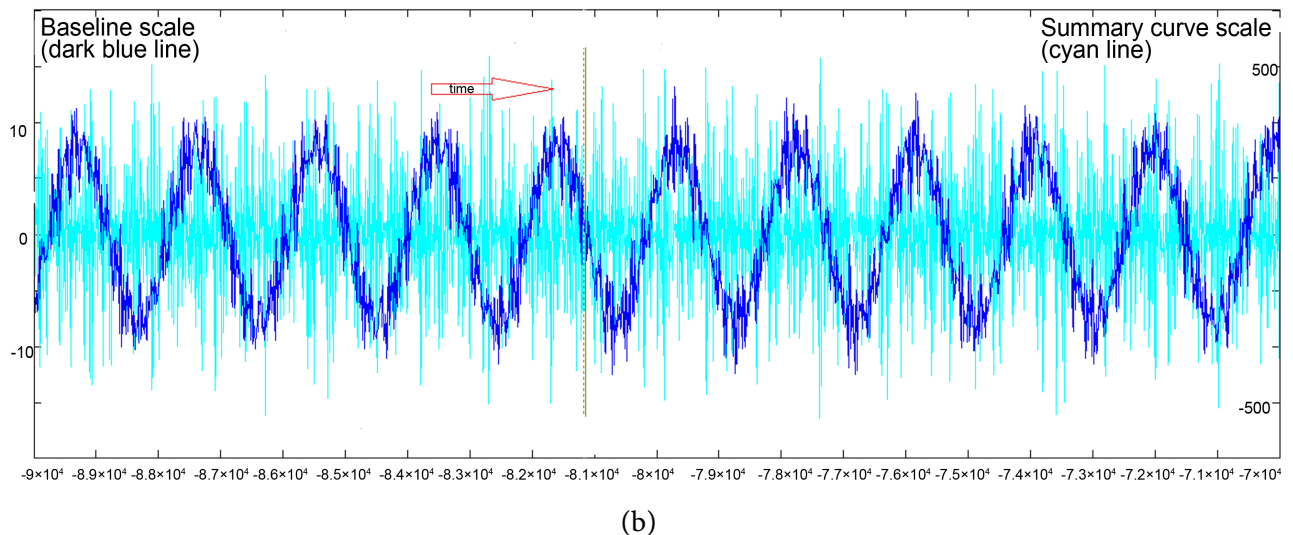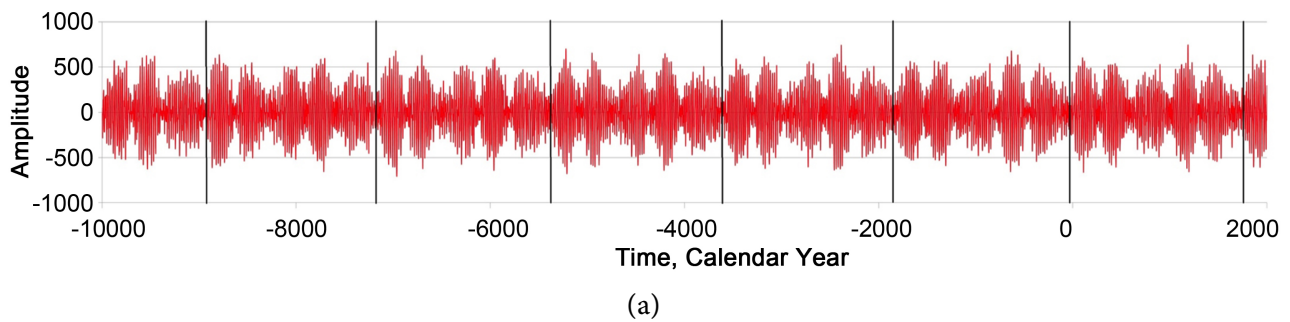
Figure 12. *Top plot*: variations of the summary curve of two magnetic field waves, or PCs (Y-axis, arbitrary units), calculated backward twelve thousand years from the current time. The vertical lines define similar patterns in five grand cycles repeated every 2000 - 2100 years (a super-grand Hallstatt's cycle). *Bottom plot*: the variations of the summary curve (cyan line) (left Y-axis, arbitrary units) calculated backward from 0 to 20 K years over-plotted by the oscillations of a magnetic field baseline, or its zero line (dark blue line) (right Y-axis, arbitrary units) with a period of about 2000 ± 95 years. The baseline oscillations are obtained with an averaging running filter of 22 years from the summary curve suppressing large-scale 11 year cycle oscillations. A courtesy of [84, 85].

4.2. Ephemeris of the Sun-Earth Distances in 600 - 2600

Let us now explore the daily Sun-Earth (S-E) distances over the two millennia (600 - 2600) derived from the ephemeris of VASOP87 - Variations Seculaires des Orbites Planetaires [90] https://neoprogrammics.com/vsop87/planetary_distance_tables/. Note that the VASOP87 data up to 6 digits after the decimal point coincide with the widely used JPL ephemeris [91]. The motion of the Earth about the barycentre of the Solar System and the Sun is demonstrated in **Figure 13** showing the elliptic orbit with two focuses F0 and F1 and the real position G of the Sun closer to the spring equinox imposed by the current position SIM [92, 93].

In this setting, the real Sun-Earth distances are shown by the green lines with respect to all the key Earth orbit positions (summer and winter solstices, spring and autumn equinoxes) of the Earth orbit. Let us present the mean monthly S-E distance variations during each sample year as plotted in **Figure 14**. This, in fact, reveals that in M1 the increases/decreases of the S-E distances (left plot) are nearly symmetric over each year and centred around the summer solstice in June and winter solstice in December while in the millennium M2 the distance curve is skewed (right plot) with the maximal Sun-Earth distances being
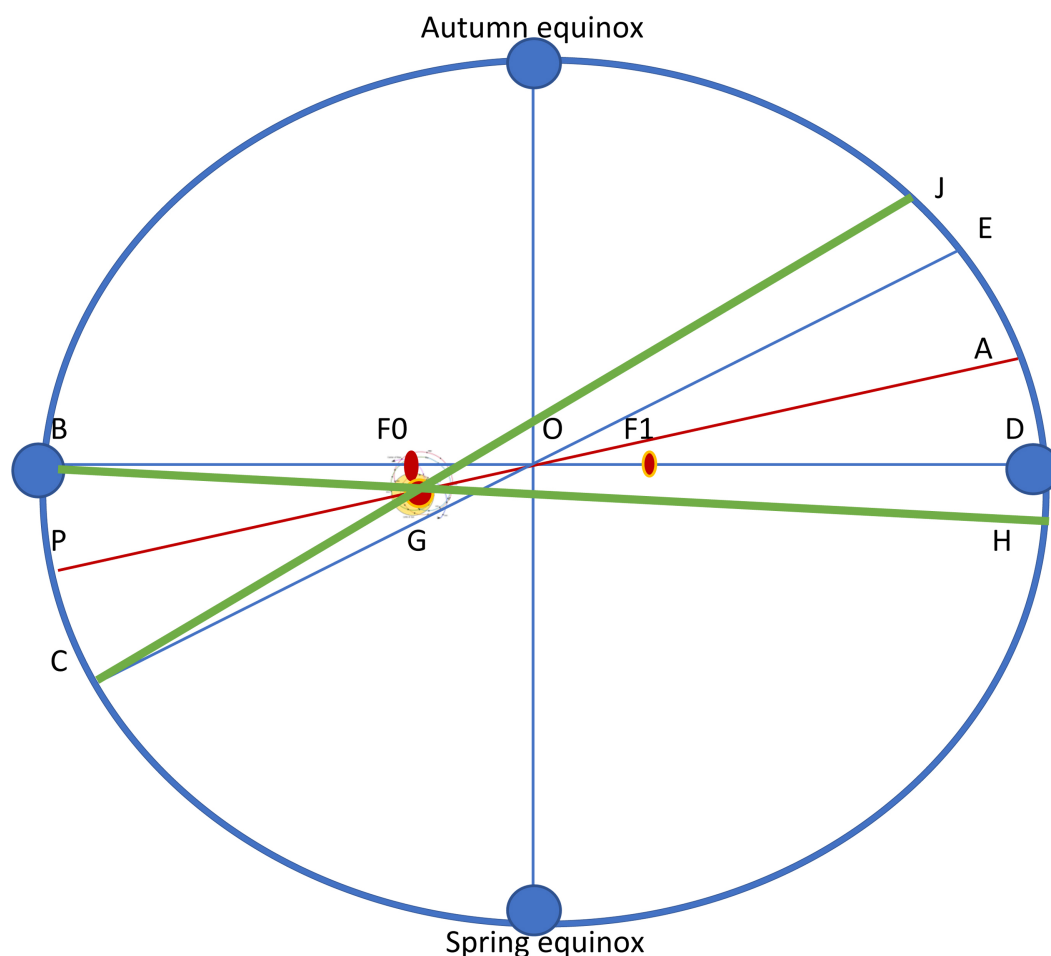
Figure 13. Orbital motion of the Earth (blue curve) about the barycentre F0 of the Solar System and the position G of the Sun defined by SIM. See the text in Section 4.2 for details.

noticeably shifted in time towards mid-July for aphelion (point A in **Figure 13**) and mid-January for perihelion (point P in **Figure 13**).

Namely, in M1 the local perihelion and local aphelion of the Earth elliptic orbit are shifted from the winter solstice on 21 December (point B in **Figure 13**) and summer solstice on 21 June (point D in **Figure 13**) forward by 5 - 6 days to 26 - 27 December (point P in **Figure 13**) and 26 - 28 June (point A in **Figure 13**), respectively. While in M2 the local perihelion and aphelion in 2600 are shifted even further from the elliptic orbit positions for the winter and summer solstices even further forward by 25 - 26 days (to 15 - 16 January for point P and 15 - 16 July for point A in **Figure 13**, respectively, as seen in the right column of Sun-Earth monthly distances shown in **Figure 5** and **Figure 6** in the chapter by Zharkova (2021) [85].

It clearly shows that the shifts in the S-E distances are reduced more in April - September and increase more in October-February of each year of millennium M2. This means that the input of solar irradiance to the Earth is not evenly distributed over the time of the Earth revolution, or over the Earth's location in the orbit.

4.3. Variations of Solar Irradiance in Two Millennia 600 - 2600

As established in [85] (their **Figures 5-9**), the Sun-Earth distances are changing rather differently from that defined by the simple revolution of Earth on the ellipse curve around the Sun as Kepler's 3rd law
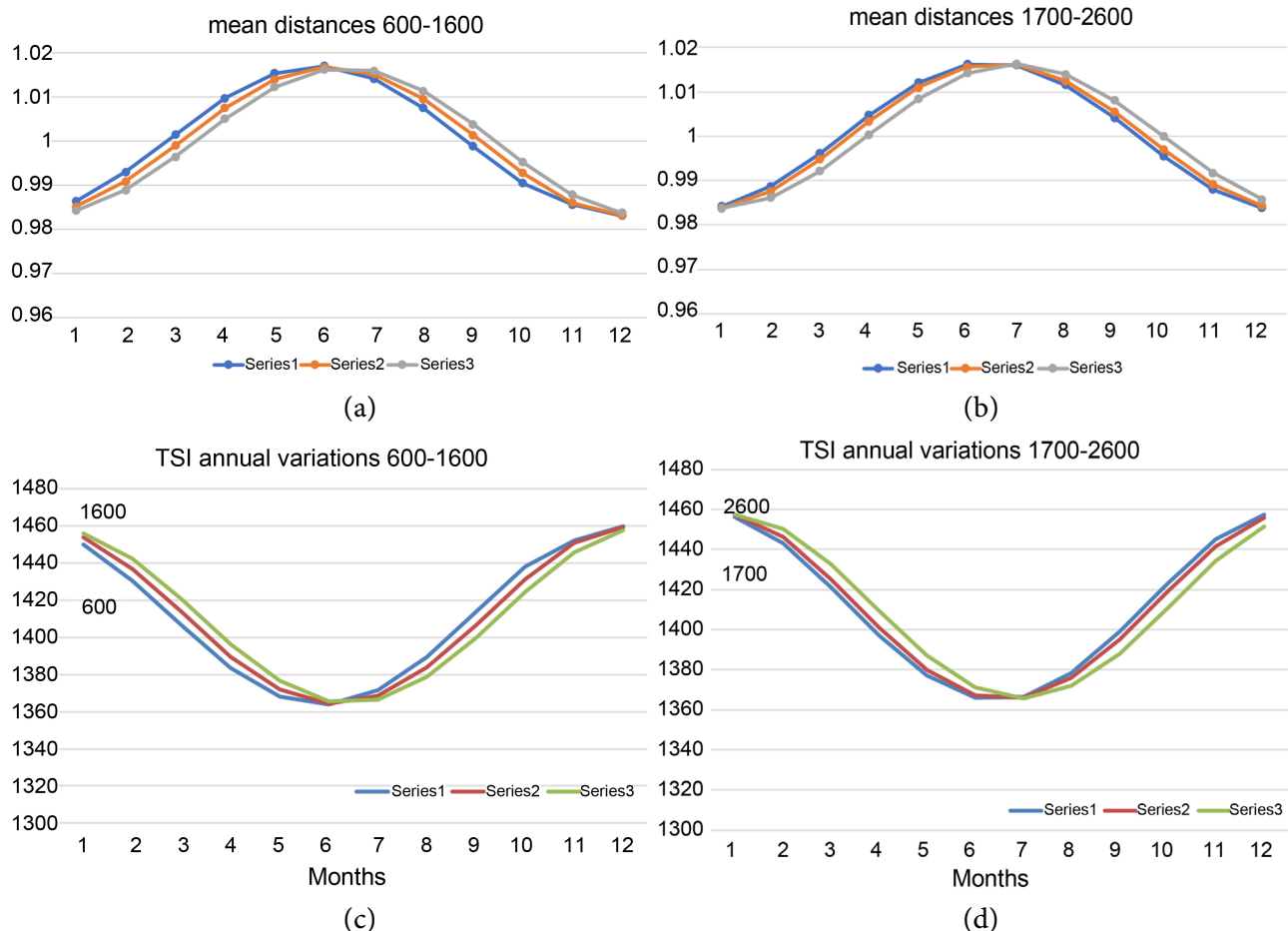
Figure 14. Top row: Variations of the annual Sun-Earth distances (axis Y, in astronomical units, au) versus months of the year (axis X) in the millennia M1 (left) and M2 (right). Left plot: blue curve - year 600, red curve - 1100, and grey curve - 1600; right plot: blue curve - 1700, red curve - 2020 and grey curve - 2600. Bottom row: The annual variations of TSI magnitudes (axis Y, in W/m²) in millennia M1 (600 - 1600) (left) and M2 (1700 - 2600) (right). Axis X shows the months of a year. All plots are courtesy of [85].

assigns. Instead, the Sun-Earth distances are defined by two motions: the Earth and the Sun about the barycentre of the solar system. The revolution of the Sun, or the sun's wobbling, is caused by the gravitational effects of large planets of the solar system, or solar inertial motion (SIM). Therefore, the daily variations of solar irradiance over a year will be affected by the combination of the Earth's revolution on its orbit and the Sun's revolution about the barycentre. The period of the first motion is one year, as we know, while the periods of the second motion vary from 173 to 2100 years.

In the millennium M1 (600 - 1600) the increase of solar irradiance during the months January-June is nearly balanced by its decrease from July to December (**Figure 11** and **Figure 12**, left column in [85]). while in M2 the solar irradiance is noticeably higher in February-July when the atmosphere is heated by the Sun than in July-December when the atmospheric cooling occurs (see **Figure 11** and **Figure 12**, right column in [85]). This is more evident in the annual variations of the monthly averaged TSI magnitudes (**Figure 14**, bottom row) revealing a steady increase of the solar irradiance input in millennia M1 and, especially, in M2, during spring-summers and decrease during autumn-winters in the Northern hemisphere in each century caused by the variations of S-E distances shown in **Figure 14**, top row, discussed above.

Hence, in the context of two-millennial periods of the TSI variations derived in section 11 from the radioisotope abundances in terrestrial biomass, the two millennial period of oscillation of the baseline magnetic field [84] and the total solar irradiance [85] derived from the full disk solar magnetograms [29, 67] have the advantage to suggest the physical mechanism for generating these oscillations, e.g. the orbital effects leading to varying Sun-Earth distances caused by the solar inertial motion induced by the gravitation of large planets [84, 85]. This mechanism gains more traction now with the similar suggestions proposed in the latest studies of solar activity with SSA method [74, 94].

4.4. Estimations of the TSI Deposited at Key Points of the Earth's Orbit

This aspect was further investigated by reference to the real S-E data pertinent to the Earth's orbit of the Sun and the timings associated with the Earth's travel path between solstice and equinox at perihelion and aphelion similar to the one presented recently [95]. Here we will refer to Figure 13 showing the Earth's schematic orbital path around the Sun. All distances measured are on the plane of the ecliptic and at an orbital eccentricity of 0.0167.

The total solar irradiation values measured here were determined at the points of perihelion, vernal and autumnal equinoxes, and aphelion in order to obtain a percentage variation that would represent the difference in received irradiation between the northern and southern hemispheres reported from observations (see, for example, [2] and references therein). Similarly to Fiori (2022) [95], for the ephemeris of the Sun-Earth distances we compare the dates and TSI obtained by Earth when it passes through its perihelion, aphelion, vernal and autumnal equinoxes, summer and winter solstices as summarised in Table 1 for years 2020 - 2022.

The total solar irradiation values measured today were determined at the key orbital points of perihelion, spring, and autumn equinoxes, and aphelion. Note that the current TSI calculations were normalised on the TSI of 1366 W/m^2 restored for the aphelion of the orbit in 1700 [96]. It is evident that the S-E distances, and thus TSI, change significantly depending on the position of the Earth on its elliptic orbit, leading to the change of seasons on Earth in different hemispheres.

The TSI received during the time from the solstice to an equivalent time past the perihelion is directed to the southern hemisphere that is experiencing summer. This time is winter in the northern hemisphere. The reverse occurs at aphelion. The difference in the timing of the summer of the southern hemisphere to the timing of the summer of the northern hemisphere is caused by the Earth's orbital velocity at the respective times. It takes longer for the earth to travel the same distance on the circumference of the ellipse during aphelion than it does during perihelion. The Earth lingers longer in the reduced irradiation from the sun at aphelion and receives about 4.7% more irradiation than the earth at perihelion, principally directed to the northern hemisphere as shown in Table 5.2 in [95].

However, these S-E distance and TSI variations are not the same for different years (2020 to 2022 as examples). it can be seen from Table 1 that the S-E distances at perihelion and autumn equinox are steadily increasing from 2020 to 2022 while at aphelion and spring equinox the S-E distances are decreasing with every year because the Sun is moving towards the spring equinox owing to SIM, or the large planet gravitation [93]. This change of S-E distances at the key points during 2020-2022, in turn, leads to the increase of TSI at Earth at the northern spring equinox and aphelion and decrease at the northern autumn equinox and perihelion. These differences between TSI keep increasing from 2020 to 2022 and during the further few centuries until at least 2500 as shown above.

Then we estimate the number of days spent by Earth between the key points of its orbit in 2020 compared to 2021 as described by [95] during the period of time when the Earth travels from the solstice to the perihelion or the aphelion and away from the perihelion or aphelion. In 2020 the time spent by the Earth between the autumn and spring equinox was 182 days and between the spring and autumn equinox was 184 days. While in 2021 these numbers become 181 and 184, respectively [95].

The amount of solar irradiance deposited on Earth in 2020 between the autumn and spring equinox when there is a summer in the Southern hemisphere and winter in the Northern one is 256,935 W/m^3, or

Table 1. The distances and solar irradiance in W/m² at the Earth key orbital points in 2020-2022.

Date	Distance, au	Distance, Mkm	TSI, W/m²	Name
5 Jan 2020	0.9832439	147.091189	1434.583956	perihelion 2020
3 Jan 2021	0.9832576	147.093245	1434.563968	perihelion 2021
4 Jan 2022	0.9833367	147.105076	1434.448571	perihelion 2022
21 Mar 2020	0.9961576	149.023060	1421.448485	spring equinox 2020
21 Mar 2021	0.9960690	149.009803	1421.701371	spring equinox 2021
21 Mar 2022	0.9959229	148.987952	1422.118523	spring equinox 2022
21 Jun 2020	1.0163050	152.037062	1365.649047	summer solstice 2020
21 Jun 2021	1.0162230	152.024802	1365.869446	summer solstice 2021
21 Jun 2022	1.0162025	152.021725	1365.924555	summer solstice 2022
4 July 2020	1.0166939	152.095236	1364.604486	aphelion 2020
6 July 2021	1.0167292	152.100524	1364.509731	aphelion 2021
4 July 2022	1.0167151	152.098417	1364.547578	aphelion 2022
21 Sep 2020	1.0040356	150.201593	1399.229673	autumn equinox 2020
21 Sep 2021	1.0040509	150.203877	1404.854997	autumn equinox 2021
21 Sep 2022	1.0041966	150.225679	1398.78104	autumn equinox 2022
21 Dec 2020	0.9837472	147.166485	1433.850001	winter solstice 2020
21 Dec 2021	0.9837636	147.168941	1433.826098	winter solstice 2021
21 Dec 2022	0.9838553	147.182660	1433.692459	winter solstice 2022

49.897% of the TSI while the amount of solar irradiance deposited between the spring and autumn equinox when summer is in Northern and winter is in Southern hemispheres reaches 257,995 W/m³, that constitutes 50.103% of overall TSI. This distribution is rather close to the estimation of 49.85% and 50.15% provided by [95] considering simplifications in their approximate method. Although, based on the findings in Section 4.3, this difference between the TSI in the opposite hemispheres is expected to increase during the next few centuries until 2500 because of a further change in the official S-E distance ephemeris supposedly caused by SIM.

A further consideration is a speed, at which the angle of obliquity changes as the Earth moves away from the summer and winter solstices as described by [95] (see Figure 5.7). The rate of change of return of the angle of obliquity from obstructing the solar irradiance at the winter solstice to the autumn equinox is smaller than the rate of change of return of the angle of obliquity from the summer solstice to the spring equinox. Thus, the angle of obliquity changes at a rate 3.8% slower at aphelion [95]. Hence the area of the Northern hemisphere is receiving solar radiation longer at aphelion than at perihelion.

Taking into consideration the characteristics of the properties and rates of the S-E distances and TSI changes in 2020 or 2021 as described here and by [95] (see their Figures 5.5, 5.6, and 5.7), the one can deduce that summers in the Northern hemisphere to last longer and to receive a greater TSI than the Southern hemisphere's summer whilst there is a longer winter in Southern hemisphere, which it receives a smaller amount of solar radiation than during the Northern hemisphere's winter. This can explain why the

polar region of the Southern hemisphere should receive less solar radiation than the polar region of the Northern hemisphere.

Fiori (2022) [95] suggested that this difference can lead to a greater probability of the Southern polar region entering into ice age conditions in the future faster than the Northern hemisphere. However, these changes could be seen on much larger timescales than the two-millennia Hallstatt's cycle discussed in the current paper.

4.5. Differences in the TSI Depositions to Earth in the Two Millennia

From the daily magnitudes of TSI shown in Figure 11 and Figure 12 of the chapter [85], it is possible to count the real distances between the Sun and Earth obtained from the official ephemeris and the total annual amount of TSI emitted by the Sun towards the Earth in each year of both millennia. If this amount does not change from year to year, then TSI is, indeed, the same for each year for both centuries, as currently assumed.

However, because in the millennia M1 (600 - 1600) and M2 (1600 - 2600) there is the shift of the maximum points of the Sun-Earth distances (Figure 14, top plots), or the minimum point of the TSI annual variations (Figure 14, bottom plots) from 21 June (M1) to 15 - 16 July (end of M2), a detectable difference occur between the annual TSI inputs in M1 and M2.

The annual magnitudes of total solar radiation (TSI) deposited to the Earth during the sampled three years (600, 1100, 1600, and 1700, 2020, 2600) in the two millennia were shown in Figure 14 [85]. These were calculated for the cases: a) by adding together the averaged monthly TSI magnitudes (left plot) calculated for the S-E distances shown in Figure 14, top plots, when only 12 magnitudes per year (for 12 months) are considered; b) by adding together the daily TSI magnitudes (right plot) taken from Figure 11 and Figure 12 of [85], associated with the daily magnitudes of TSI (for 366 days for the leap years).

These two plots clearly demonstrated [85] that the monthly TSI variations (case a) show the increase of TSI by about 1 - 1.3 W/m^2 in 2020 compared to 1700. This TSI increase found from the S-E distance ephemeris is close to the magnitude of 1 - 1.5 W/m^2 reported from the current TSI observations [97]. However, it was shown that the annual TSI magnitudes, calculated from the daily S-E distances (case b) reveal much larger annual increases of the TSI by about 20 - 25 W/m^2 (>1.8%) in M2 than in millennium M1.

This indicates that the averaged TSI will increase in M2 by about 2.5 - 2.8 W/m^2 per century, or (0.18% - 0.20%), compared to the TSI in 1700. This calculation uncovers a hidden TSI input present in millennium M2 (1600 - 2600), which is likely caused by the gravitational effects of large planets, or solar inertial motion. This effect is significantly underestimated if only the averaged monthly TSI magnitudes are used (compare here Figure 14, bottom left and right plots) as well as Figure 14, top and bottom plots, in the chapter [85]). The important issue is how this extra solar radiation is distributed between the hemispheres during the Earth revolution about the barycentre or the level of exposure of the Earth to solar radiation during different seasons and different positions of the Earth orbit parameters [98, 99].

Furthermore, it was shown that the distribution of the TSI to the opposite hemispheres varies during a year. At the start of any year when the Earth is turned to the Sun with its Southern hemisphere, any decrease and increase of solar radiation occurring during this time are mostly absorbed by the Southern hemisphere. When the Earth's orbit approaches the spring equinox in March, the distribution of TSII between the hemispheres becomes nearly even, while in April-July the main part of the solar radiation input is shifted toward the Northern hemisphere. Theoretically (by Kepler's law), the Earth aphelion should occur on the summer solstice, 21 June, while, in reality, it is shifted to 5 July in 2020 and to 16 July in 2500.

Hence, because of the shift of the Sun towards the spring equinox position of the Earth orbit owing to the gravitation of large planets, in the millennium M2 the Northern hemisphere should get the extra solar radiation not only in the first six months of a year but especially, in the 25 days between 21 June and 16 July when the aphelion is approached in 2500. This extra TSI deposited to the Earth for the Northern hemispheres in the spring and summer is not compensated later in autumn and winter. This is possibly af-

fecting to some extent the Southern hemisphere as well because of extra cooling occurring because of a shift of the local perihelion to 16 January in 2500.

Therefore, the deposition of TSI in the millennium M2 can be essentially higher than in millennium M1. This can lead to different seasonal changes in the opposite hemispheres because of the uneven shifts of Sun-Earth distances on the orbit owing to SIM. This extra input of the TSI amount caused by SIM (from the variations of a distance d in inverse squares formula for solar radiation) will undoubtedly add to the magnitude of solar heating coming from the solar activity itself as shown in **Figure 4** (bottom plot, blue lines) in [85]. This, in turn, can account for a large solar input to the terrestrial temperature increase shown by the red curves in **Figure 4**, bottom plot, red lines) in [85], in addition to any other natural and anthropogenic causes considered so far.

5. DISCUSSION AND CONCLUSIONS

5.1. Derived Periods and Their Links to Solar Activity and Orbital Motion

In this paper we carried out spectral analysis with the wavelet and Fourier transforms for the averaged sunspot numbers representing the toroidal magnetic field of the solar dynamo and the summary curve derived from the two largest eigenvectors derived from solar background magnetic field representing a poloidal magnetic field of the solar dynamo. Despite differences between the proxies of solar activity used, we established that the key period of solar activity is 11-years (or 10.7-years to be precise) and it is the same for both proxies. There is also a period of about 22 years, or 21.4 years to be precise, detected from the summary curve of eigenvectors of SBMF where the polarity of the magnetic field is taken into account. These periods are derived from the sunspot numbers, summary, and modulus summary curves of eigenvectors of magnetic waves generated by dipole magnetic sources.

There was another period detected in the sunspot data of about 101 years, or the Gleissberg's cycle, which does not appear in the modulus summary curve of the two largest eigenvectors generated by dipole magnetic sources. This is understood during the interpretation of the observed activity when Gleissberg's cycle can be accounted for from consideration of the next pair of eigenvectors generated by quadruple magnetic sources. Some other weaker periods of 40 - 60 years were detected in the global wavelet spectrum on the edge of 95% confidence interval or in Fourier spectrum that can be accountable for the period of 44 years in the variations of sunspot diameters derived from the cycles 12 - 24 [65].

This finding allows us to confirm the conclusion of the other authors that the key period of solar activity is a 11/22-year cycle [3, 6], while other periods could be a simple interference of the basic waves produced by the solar dynamo in two layers with different magnetic sources: dipole, quadruple, sextuple or octuple. Such the interference of two waves from dipole magnetic sources reveals the important period of 342 - 344 years detected from the summary, modulus summary curves of eigenvectors of dipole magnetic waves in the 2000 years (1200 - 3200). This reflects the average of the five periods ranging from 330 to 380 years, constituting five grand solar cycles (GSCs) separated by four grand solar minima (GSMs).

This grand solar cycle period of 342 - 344 years is likely caused by the wave interference (beating effect) of the two largest eigenvectors [29]. The similar grand period of 350 years was also recorded in the wavelet and Fourier spectra of the solar irradiance derived from the carbon14 isotope abundances in the biomass in the past 12,000 years [40]. This grand period of 330 - 380 years is well recorded in the past observations of solar activity via numerous GSMs: Maunder, Wolf, Oort, Homeric, and other grand solar minima.

The fact that eigenvectors come in pairs assumes that these waves are formed in different layers of the solar interior, which have different properties and thus produce the dynamo waves with the close but not equal frequencies (or periods) and the phase difference between these two waves varying in time as a cosine function. We explored the opportunity of these dynamo waves to be formed by the dynamo action in two layers with slightly different velocities of meridional circulation that induces the beating effect during the wave interference and forms these grand solar cycles like those beats appearing when tuning a piano with a fork.

Furthermore, because these two dynamo waves are formed in different layers (one in the solar interior near the bottom of the solar convective zone and another close to the shallow layer beneath the surface, this allows us to reconcile the existing dynamo models considering some stochasticity of the waves in the shallow layer caused by its properties and another stochasticity appearing naturally from the phase difference between the waves that can explain essential features of the solar dynamo waves.

The other, larger, period, which was reported from the observation of solar radiations recorded in the abundances of the isotope of carbon 14 in the terrestrial biomass, was the two millennial period of 2200 - 2300 years which also coincided with the period of oscillations of the magnetic field baseline derived directly from the summary curve. Since none of the dynamo models can account for any oscillations of the zero line of a magnetic field, we looked at the cause of this oscillation in the orbits of the solar planets and the sun itself, shifting from the ellipse focus towards the Earth's orbit points (currently, towards the spring equinox point), so-called solar inertial motion. This SIM causes standard deposition of solar radiation in one millennium (600 - 1600) and much stronger deposition of solar radiations in the other millennium (1600 - 2600) independently on solar activity processes in the Sun itself.

By comparing all these periods together one can understand better the effects of not only solar activity but also the interaction of the Sun with the planets of the Solar System and their effects on the terrestrial temperature.

5.2. TSI Variations and Terrestrial Temperature

Let us try to evaluate how these variations of solar irradiance can affect terrestrial temperature from the general similarity approach using the plot presented in Figure 15, courtesy of [100]. The variations of the temperature have a decadal trend linked to 11-year cycles and the baseline variations linked to other mechanisms of solar irradiance variations (grand solar minima [1, 29], solar inertial motion [41, 85, 101], other orbital variations caused by Milankovich cycles [98].

The TSI variations caused by the solar activity in normal cycles of the 11 years and during grand solar minima (similar to the Maunder Minimum, MM) can be described as follows.

1) Solar irradiance S variations at Earth owing to 11 year cycle is about 0.1% of the average magnitude of TSI S (1366 Wm^{-2} accepted in this study) increasing by 1.4 Wm^{-2} during maxima and decreasing during minima [102, 103]. These estimations are also supported by the other researchers [104, 105] showing sometimes up to 0.4% contributions of active regions into the solar radiance intensity.
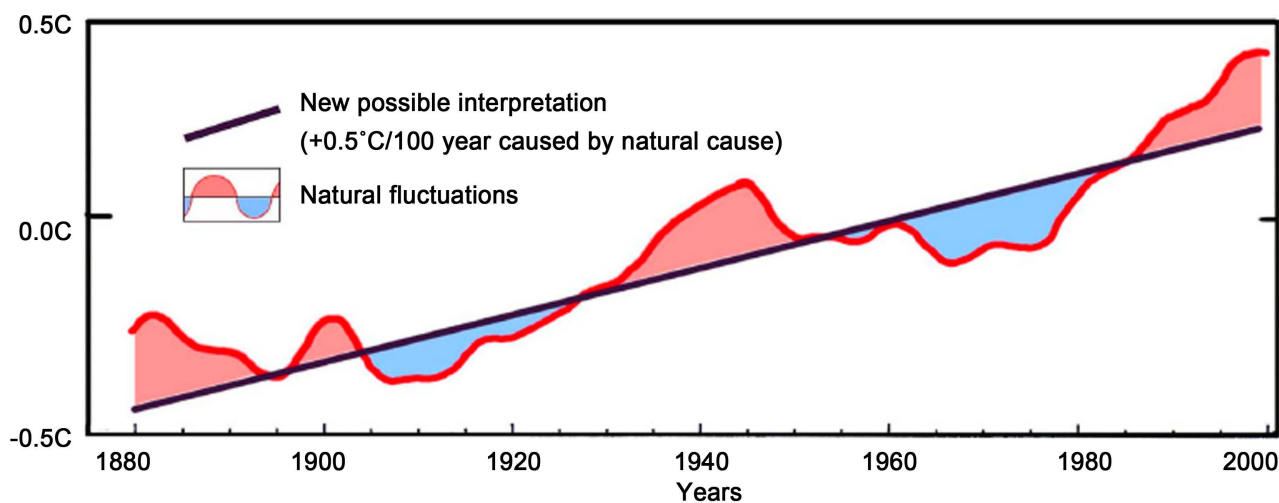
Figure 15. Terrestrial temperature variations from 1880 until 2000 showing the increase of the baseline temperature (solid black line over imposed by the decadal oscillations shown by the blue (decreasing) and red (increasing) shapes. A courtesy of [100].

The terrestrial temperature variations during 11-year cycle are small but noticeable as shown by decadal variations in Figure 15 being proportional to the averaged sunspot numbers [1, 106, 107] and many terrestrial factors like variations of ocean temperature, directions off jets and ENSO variations with El Nino and La Nina events [2]. This leads to recognisable increases of the terrestrial temperature during or close to the maxima of solar activity and decreases during or close to the minima.

2) Solar irradiance S variations (decreases) at Earth owing to GSM is about 2.5 - 3 W/m^2, or 0.22% of S [96, 105, 108] as shown in Figure 2 (top plot) in [85]. This would lead to recognisable decreases of the baseline temperatures during GSMs, similar to that reported for the Maunder Minimum [109-111].

The terrestrial temperature curve averaged from the fluctuations in 11-year cycles presented in Figure 2 (bottom plot) in [85] shows a reduction during the MM of the average terrestrial temperature by about 1.0˚C [109-111], e.g. the decrease of TSI by 0.11% secures a decrease of the terrestrial temperature by approximately 0.5˚C.

5.3. Effects of the Upcoming Grand Solar Minimum (2020 - 2053)

In the next 30 years, the Sun is entering a period of reduced solar activity, the modern grand solar minimum [29], which can be called a "mini ice age", similar to the Maunder Minimum. This is already confirmed by the sharpest increase of spotless days in cycle 25 compared to all other cycles [30, 64], or by a sharp increase of the methane index in the terrestrial atmosphere supposedly caused by a decrease of the UV radiation of the Sun igniting a decrease of the terrestrial ozone abundances caused by it [112]. There were also signs of the reducing terrestrial temperature recorded in the past decades until the minimum between cycles 24 and 25 [2, 113-115], which now are overridden by an increase of this temperature that is likely [107] caused by the approaching maximum of cycle 25 combined with the effect of the solar inertial motion on the baseline temperature [85, 100].

Given that cycle 25 is still at its maximum, further confirmation of the reduction of solar activity and its effect on the terrestrial atmosphere will come during the next decade, in the descending phase of cycle 25 and the solar minimum between cycles 25 and 26. This is when the full grand solar minimum will occur in the Sun leading to a significantly reduced solar magnetic field on the solar surface caused by the disruptive interference of two magnetic waves generated by the double dynamo in the solar interior [29]. Since the SIM effects have a long period of 2200 - 2300 years [41, 84, 85], then, it will not change much a deposition of solar radiation to the Earth within 30 years of GSM, it will be mainly defined by the GSM. The first modern GSM1 occurs in 2020 - 2053 [29, 34] with the cycle amplitudes reduction to 80% in cycle 25, to 30% in cycle 26 and to 70% in cycle 27 from the maximum amplitude of cycle 24. The second modern GSM2 will happen in 2370 - 2415 [29, 34].

Because solar irradiance and the terrestrial temperature already increased since the MM as is clearly recorded from the terrestrial temperature variations [100, 107], the terrestrial temperature during the first modern GSM1 is expected to drop by about 1.0˚C to become just 0.5˚C higher than it was in 1700. The second GSM2 will arrive in 2375 - 2415 [29] and because at this time the Sun will move closer towards the Earth owing to SIM [84, 85], the starting terrestrial temperature before GSM2 will be higher by 1.5˚C than at the start of the current GSM1. The reduction of TSI caused by solar activity in GSM2 will lead to a reduction of the terrestrial temperature by 1.0˚C, leaving the Earth warmer by about 0.5˚C during the GSM2 compared to the temperature at the end of the current GSM1, or by 1.0˚C higher than in 1700.

Therefore, the periods of solar activity of 10.7, 21.5, 350, and 2100 - 2300 years derived from the variations of averaged sunspot numbers, eigenvectors of SBMF and solar irradiance linked to isotope abundances can jointly help us to understand better the solar activity on short and long timescales, provide some plausible logical interpretation and anticipate their expected effects on the terrestrial environment.

(SIDC) at the Royal Observatory of Belgium for providing the corrected averaged sunspot numbers. The authors also express their deepest gratitude to the staff and directorate of Wilcox Solar Observatory for providing the coherent long-term observations of full disk synoptic maps of the solar background magnetic field. All the authors wish also to acknowledge the support of the ZVS Research Enterprise Ltd., UK.

CONFLICTS OF INTEREST

The authors declare no conflicts of interest regarding the publication of this paper.

REFERENCES

1. Eddy, J.A. (1976) The Maunder Minimum. *Science*, **192**, 1189-1202. https://doi.org/10.1126/science.192.4245.1189

2. Connolly, R., *et al.* (2021) How Much Has the Sun Influenced Northern Hemisphere Temperature Trends? An Ongoing Debate. *Research in Astronomy and Astrophysics*, **21**, 131. https://doi.org/10.1088/1674-4527/21/6/131

3. Cameron, R.H. and Schüssler, M. (2017) Understanding Solar Cycle Variability. *Astrophysical Journal*, **843**, 111. https://doi.org/10.3847/1538-4357/aa767a

4. Usoskin, I.G., Gallet, Y., Lopes, F., Kovaltsov, G.A. and Hulot, G. (2016) Solar Activity during the Holocene: The Hallstatt Cycle and Its Consequence for Grand Minima and Maxima. *Astronomy and Astrophysics*, **587**, A150. https://doi.org/10.1051/0004-6361/201527295

5. Usoskin, I.G., *et al.* (2021) Solar Cyclic Activity over the Last Millennium Reconstructed from Annual ¹⁴C Data. *Astronomy and Astrophysics*, **649**, A141. https://doi.org/10.1051/0004-6361/202140711

6. Cameron, R.H. and Schüssler, M. (2019) Solar Activity: Periodicities beyond 11 Years Are Consistent with Random Forcing. *Astronomy and Astrophysics*, **625**, A28. https://doi.org/10.1051/0004-6361/201935290

7. Brehm, N., *et al.* (2021) Eleven-Year Solar Cycles over the Last Millennium Revealed by Radiocarbon in Tree Rings. *Nature Geoscience*, **14**, 10-15. https://doi.org/10.1038/s41561-020-00674-0

8. Hale, G.E., Ellerman, F., Nicholson, S.B. and Joy, A.H. (1919) The Magnetic Polarity of Sun-Spots. *Astrophysical Journal*, **49**, 153. https://doi.org/10.1086/142452

9. Parker, E.N. (1955) Hydromagnetic Dynamo Models. *Astrophysical Journal*, **122**, 293. https://doi.org/10.1086/146087

10. Babcock, H.W. (1961) The Topology of the Sun's Magnetic Field and the 22-YEAR Cycle. *Astrophysical Journal*, **133**, 572. https://doi.org/10.1086/147060

11. Jones, C.A., Thompson, M.J. and Tobias, S.M. (2010) The Solar Dynamo. *Space Science Review*, **152**, 591-616. https://doi.org/10.1007/s11214-009-9579-5

12. Parker, E.N. (1993) A Solar Dynamo Surface Wave at the Interface between Convection and Nonuniform Rotation. *Astrophysical Journal*, **408**, 707-719. https://doi.org/10.1086/172631

13. Leighton, R.B. (1969) A Magneto-Kinematic Model of the Solar Cycle. *Astrophysical Journal*, **156**, 1. https://doi.org/10.1086/149943

14. Choudhuri, A.R., Schussler, M. and Dikpati, M. (1995) The Solar Dynamo with Meridional Circulation. *Astronomy and Astrophysics*, **303**, L29.

15. Dikpati, M. and Choudhuri, A.R. (1995) On the Large-Scale Diffuse Magnetic Field of the Sun. *Solar Physics*, **161**, 9-27. https://doi.org/10.1007/BF00732081

16. Spiegel, E.A. and Weiss, N.O. (1980) Magnetic Activity and Variations in Solar Luminosity. *Nature*, **287**, 616-617. https://doi.org/10.1038/287616a0

17. Jones, C.A., Weiss, N.O. and Cattaneo, F. (1985) Nonlinear Dynamos: A Complex Generalization of the Lorenz Equations. *Physica D Nonlinear Phenomena*, **14**, 161-176. https://doi.org/10.1016/0167-2789(85)90176-9

18. Covas, E., Tavakol, R. and Moss, D. (2001) Dynamical Variations of the Differential Rotation in the Solar Convection Zone. *Astronomy and Astrophysics*, **371**, 718-730. https://doi.org/10.1051/0004-6361:20010345

19. Miesch, M.S. and Toomre, J. (2009) Turbulence, Magnetism, and Shear in Stellar Interiors. *Annual Review of Fluid Mechanics*, **41**, 317-345. https://doi.org/10.1146/annurev.fluid.010908.165215

20. Brun, A.S. and Rempel, M. (2009) Large Scale Flows in the Solar Convection Zone. *Space Science Review*, **144**, 151-173. https://doi.org/10.1007/s11214-008-9454-9

21. Weiss, N.O. (1990) Solar and Stellar Convection Zones. *Computer Physics Reports*, **12**, 233-245. https://doi.org/10.1016/0167-7977(90)90012-U

22. Tobias, S.M. (2002) The Solar Dynamo. *Royal Society of London Philosophical Transactions Series A*, **360**, 2741-2756. https://doi.org/10.1098/rsta.2002.1090

23. Schmitt, D. and Schuessler, M. (1989) Non-Linear Dynamos. I. One-Dimensional Model of a Thin Layer Dynamo. *Astronomy and Astrophysics*, **223**, 343-351. https://doi.org/10.12942/lrsp-2010-3

24. Charbonneau, P. (2010) Dynamo Models of the Solar Cycle. *Living Reviews in Solar Physics*, **7**, 3.

25. Tobias, S.M., Cattaneo, F. and Boldyrev, S. (2011) MHD Dynamos and Turbulence. Cambridge University Press, Cambridge. https://doi.org/10.1017/CBO9781139032810.010

26. Charbonneau, P. (2014) Solar Dynamo Theory. *Annual Review of Astronomy and Astrophysics*, **52**, 251-290. https://doi.org/10.1146/annurev-astro-081913-040012

27. Nigro, G., Pongkitiwanichakul, P., Cattaneo, F. and Tobias, S.M. (2017) What Is a Large-Scale Dynamo? *Monthly Notices of RAS*, **464**, L119-L123. https://doi.org/10.1093/mnrasl/slw190

28. Zharkova, V.V., Shepherd, S.J. and Zharkov, S.I. (2012) Principal Component Analysis of Background and Sunspot Magnetic Field Variations during Solar Cycles 21-23. *Monthly Notices of RAS*, **424**, 2943-2953. https://doi.org/10.1111/j.1365-2966.2012.21436.x

29. Zharkova, V.V., Shepherd, S.J., Popova, E. and Zharkov, S.I. (2015) Heartbeat of the Sun from Principal Component Analysis and Prediction of Solar Activity on a Millenium Timescale. *Nature Scientific Reports*, **5**, 15689. https://doi.org/10.1038/srep15689

30. Zharkova, V.V. and Shepherd, S.J. (2022) Eigen Vectors of Solar Magnetic Field in Cycles 21-24 and Their Links to Solar Activity Indices. *Monthly Notices of the Royal Astronomical Society*, **512**, 5085-5099. https://doi.org/10.1093/mnras/stac781

31. Lawrence, J.K., Cadavid, A. and Ruzmaikin, A. (2004) Principal Component Analysis of the Solar Magnetic Field I: The Axisymmetric Field at the Photosphere. *Solar Physics*, **225**, 1-19. https://doi.org/10.1007/s11207-004-3257-2

32. Cadavid, A.C., Lawrence, J.K., McDonald, D.P. and Ruzmaikin, A. (2005) Independent Global Modes of Solar Magnetic Field Fluctuations. *Solar Physics*, **226**, 359-376. https://doi.org/10.1007/s11207-005-8187-0

33. Zharkov, S., Gavryuseva, E. and Zharkova, V. (2008) The Observed Long- and Short-Term Phase Relation between the Toroidal and Poloidal Magnetic Fields in Cycle 23. *Solar Physics*, **248**, 339-358. https://doi.org/10.1007/s11207-007-9109-0

34. Zharkova, V. (2020) Modern Grand Solar Minimum Will Lead to Terrestrial Cooling. *Temperature*, **7**, 217-222. https://doi.org/10.1080/23328940.2020.1796243

35. Zharkova, V., Vasilieva, I., Shepherd, S.J. and Popova, E. (2022) Comparison of Solar Activity Proxies: Eigen Vectors versus Averaged Sunspot Numbers.

36. Popova, E., Zharkova, V., Shepherd, S. and Zharkov, S. (2018) On a Role of Quadruple Component of Magnetic Field in Defining Solar Activity in Grand Cycles. *Journal of Atmospheric and Solar-Terrestrial Physics*, **176**, 61-68. https://doi.org/10.1016/j.jastp.2017.05.006

37. Reimer, P., *et al.* (2009) INTCAL09 And MARINE09 Radiocarbon Age Calibration Curves 0-50 000 Years CAL BP. *Radiocarbon*, **51**, 1111-1150. https://doi.org/10.1017/S0033822200034202

38. Vieira, L.E.A., Solanki, S.K., Krivova, N.A. and Usoskin, I. (2011) Evolution of the Solar Irradiance during the Holocene. *Astronomy and Astrophysics*, **531**, A6. https://doi.org/10.1051/0004-6361/201015843

39. Vieira, L.E.A., Solanki, S.K., Krivova, N.A. and Usoskin, I. (2011) VizieR Online Data Catalog: Evolution of Solar Irradiance during Holocene (Vieira+, 2011). VizieR Online Data Catalog J/A+A/531/A6.

40. Steinhilber, F., *et al.* (2012) 9,400 Years of Cosmic Radiation and Solar Activity from Ice Cores and Tree Rings. *Proceedings of the National Academy of Science*, **109**, 5967-5971. https://doi.org/10.1073/pnas.1118965109

41. Scafetta, N., Milani, F., Bianchini, A. and Ortolani, S. (2016) On the Astronomical Origin of the Hallstatt Oscillation Found in Radiocarbon and Climate Records throughout the Holocene. *Earth Science Reviews*, **162**, 24-43. https://doi.org/10.1016/j.earscirev.2016.09.004

42. Mazzarella, A. and Palumbo, A. (1989) Does the Solar Cycle Modulate Seismic and Volcanic Activity. *Journal of Volcanology and Geothermal Research*, **39**, 89-93. https://doi.org/10.1016/0377-0273(89)90023-1

43. Farge, M. (1992) Wavelet Transforms and Their Applications to Turbulence. *Annual Review of Fluid Mechanics*, **24**, 395-458. https://doi.org/10.1146/annurev.fl.24.010192.002143

44. Terrence, C. and Campo, G.P. (1998) A Practical Guide to Wavelet Analysis. *Bulletin of the American Meteorological Society*, **79**, 61-78. https://doi.org/10.1175/1520-0477(1998)079<0061:APGTWA>2.0.CO;2

45. Bruns, A. (2004) Fourier-, Hilbert- and Wavelet-Based Signal Analysis: Are They Really Different Approaches? *Journal of Neuroscience Methods*, **137**, 321-332. https://doi.org/10.1016/j.jneumeth.2004.03.002 https://www.sciencedirect.com/science/article/pii/S0165027004001098

46. Aguilar-Rodriguez, E., *et al.* (2015) Comparison of Solar Wind Speeds Using Wavelet Transform and Fourier Analysis in IPS Data. *Solar Physics*, **290**, 2507-2518. https://doi.org/10.1007/s11207-015-0758-0

47. Thomas, E. and Abraham, N.P. (2022) Relationship between Sunspot Number and Seasonal Rainfall over Kerala Using Wavelet Analysis. *Journal of Atmospheric and Solar-Terrestrial Physics*, **240**, Article ID: 105943. https://doi.org/10.1016/j.jastp.2022.105943

48. Wolf, R. (1877) Geschichte der Astronomie. Oldenbourg Wissenschaftsverlag, Munich. https://doi.org/10.1515/9783486724479

49. Hoyt, D.V. and Schatten, K.H. (1998) Group Sunspot Numbers: A New Solar Activity Reconstruction. *Solar Physics*, **179**, 189-219. https://doi.org/10.1023/A:1005007527816

50. Hoyt, D.V. and Schatten, K.H. (1998) Group Sunspot Numbers: A New Solar Activity Reconstruction. *Solar Physics*, **181**, 491-512. https://doi.org/10.1023/A:1005056326158

51. Hoyt, D.V., Schatten, K.H. and Nesme-Ribes, E. (1994) The One Hundredth Year of Rudolf Wolf's Death: Do We Have the Correct Reconstruction of Solar Activity? *Geophysics Research Letters*, **21**, 2067-2070. https://doi.org/10.1029/94GL01698

52. Clette, F., Svalgaard, L., Vaquero, J.M. and Cliver, E.W. (2014) Revisiting the Sunspot Number. A 400-Year Perspective on the Solar Cycle. *Space Science Review*, **186**, 35-103. https://doi.org/10.1007/s11214-014-0074-2

53. Velasco Herrera, V.M., Soon, W. and Legates, D.R. (2021) Does Machine Learning Reconstruct Missing Sunspots and Forecast a New Solar Minimum? *Advances in Space Research*, **68**, 1485-1501. https://doi.org/10.1016/j.asr.2021.03.023

54. Leussu, R., Usoskin, I.G., Arlt, R. and Mursula, K. (2013) Inconsistency of the Wolf Sunspot Number Series around 1848. *Astronomy and Astrophysics*, **559**, A28. https://doi.org/10.1051/0004-6361/201322373

55. Usoskin, I.G., Mursula, K., Solanki, S., Schüssler, M. and Alanko, K. (2004) Reconstruction of Solar Activity for the Last Millennium Using ^{10}Be Data. *Astronomy and Astrophysics*, **413**, 745-751. https://doi.org/10.1051/0004-6361:20031533

56. Vaquero, J.M., Gallego, M.C. and Trigo, R.M. (2007) Sunspot Numbers during 1736 1739 Revisited. *Advances in Space Research*, **40**, 1895-1903. https://doi.org/10.1016/j.asr.2007.02.097

57. Vaquero, J.M. (2007) Historical Sunspot Observations: A Review. *Advances in Space Research*, **40**, 929-941. https://doi.org/10.1016/j.asr.2007.01.087

58. Vaquero, J.M. and Gallego, M.C. (2014) Reconstructing Past Solar Activity Using Meridian Solar Observations: The Case of the Royal Observatory of the Spanish Navy (1833-1840). *Advances in Space Research*, **53**, 1162-1168. https://doi.org/10.1016/j.asr.2014.01.015

59. Svalgaard, L. and Schatten, K.H. (2016) Reconstruction of the Sunspot Group Number: The Backbone Method. *Solar Physics*, **291**, 2653-2684. https://doi.org/10.1007/s11207-015-0815-8

60. Svalgaard, L. and Schatten, K.H. (2017) On the Sunspot Group Number Reconstruction: The Backbone Method Revisited.

61. Svalgaard, L. and Schatten, K.H. (2017) Sunspot Group Numbers since 1900 and Implications for the Long-Term Record of Solar Activity.

62. Carrasco, V.M.S., Gallego, M.C. and Vaquero, J.M. (2020) Number of Sunspot Groups from the Galileo-Scheiner Controversy Revisited. *Monthly Notices of RAS*, **496**, 2482-2492. https://doi.org/10.1093/mnras/staa1633

63. Hayakawa, H., *et al.* (2020) Sunspot Observations by Hisako Koyama: 1945-1996. *Monthly Notices of RAS*, **492**, 4513-4527. https://doi.org/10.1093/mnras/stz3345

64. SILSO World Data Center (2021) The International Sunspot Number. International Sunspot Number Monthly Bulletin and Online Catalogue. https://www.sidc.be/silso/datafiles

65. Efimenko, V.M. and Lozitsky, V.G. (2018) Essential Features of Long-Term Changes of Areas and Diameters of Sunspot Groups in Solar Activity Cycles 12-24. *Advances in Space Research*, **61**, 2820-2826. https://doi.org/10.1016/j.asr.2018.03.012

66. Stix, M. (1976) Differential Rotation and the Solar Dynamo. *Astronomy and Astrophysics*, **47**, 243-254.

67. Shepherd, S.J., Zharkov, S.I. and Zharkova, V.V. (2014) Prediction of Solar Activity from Solar Background Magnetic Field Variations in Cycles 21-23. *Astrophysical Journal*, **795**, 46. https://doi.org/10.1088/0004-637X/795/1/46

68. Schmidt, M. and Lipson, H. (2009) Distilling Free-Form Natural Laws from Experimental Data. *Science*, **324**, 81-85. https://doi.org/10.1126/science.1165893

69. Popova, E., Zharkova, V. and Zharkov, S. (2013) Probing Latitudinal Variations of the Solar Magnetic Field in Cycles 21-23 by Parker's Two-Layer Dynamo Model with Meridional Circulation. *Annales Geophysicae*, **31**, 2023-2038. https://doi.org/10.5194/angeo-31-2023-2013

70. Zharkova, V.V., Shepherd, S.J., Popova, E. and Zharkov, S.I. (2018) Reinforcing a Double Dynamo Model with Solar-Terrestrial Activity in the Past Three Millennia. In: Foullon, C. and Malandraki, O.E., Eds., *Space Weather of the Heliosphere: Processes and Forecasts*, Vol. 335, International Astronomical Union, Brussels, 211-215. https://doi.org/10.1017/S1743921317010912

71. Zharkova, V.V., Shepherd, S.J., Popova, E. and Zharkov, S.I. (2018) Reply to Comment on the Paper "Popova *et al* on a Role of Quadruple Component of Magnetic Field in Defining Solar Activity in Grand Cycles" by Usoskin

(2018). *Journal of Atmospheric and Solar-Terrestrial Physics*, **176**, 72-82. https://doi.org/10.1016/j.jastp.2017.09.019

72. Kitiashvili, I.N. (2020) Application of Synoptic Magnetograms to Global Solar Activity Forecast. *Astrophysical Journal*, **890**, 36. https://doi.org/10.3847/1538-4357/ab64e7

73. Obridko, V.N., Sokoloff, D.D., Pipin, V.V., Shibalvaa, A.S. and Livshits, I.M. (2021) Zonal Harmonics of Solar Magnetic Field for Solar Cycle Forecast. *Journal of Atmospheric and Solar-Terrestrial Physics*, **225**, Article ID: 105743. https://doi.org/10.1093/mnras/stab1062

74. Courtillot, V., Lopes, F. and Le Mouël, J.L. (2021) On the Prediction of Solar Cycles. *Solar Physics*, **296**, 21. https://doi.org/10.1007/s11207-020-01760-7

75. Zhao, J., Bogart, R.S., Kosovichev, A.G., Duvall, T.L. and Hartlep, T. (2013) Detection of Equatorward Meridional Flow and Evidence of Double-Cell Meridional Circulation inside the Sun. *Astrophysical Journal Letters*, **774**, L29. https://doi.org/10.1088/2041-8205/774/2/L29

76. Ruzmaikin, A.A. (1981) The Solar Cycle as a Strange Attractor. *Comments on Astrophysics*, **9**, 85-93.

77. Kitiashvili, I. and Kosovichev, A.G. (2008) Application of Data Assimilation Method for Predicting Solar Cycles. *Astrophysical Journal Letters*, **688**, L49. https://doi.org/10.1086/594999

78. Kitiashvili, I.N. and Kosovichev, A.G. (2009) Nonlinear Dynamical Modeling of Solar Cycles Using Dynamo Formulation with Turbulent Magnetic Helicity. *Geophysical and Astrophysical Fluid Dynamics*, **103**, 53-68. https://doi.org/10.1080/03091920802396518

79. Popova, E.P. and Potemina, K.A. (2013) Modeling of the Solar Activity Double Cycle Using Dynamical Systems. *Geomagnetism and Aeronomy*, **53**, 941-944. https://doi.org/10.1134/S0016793213080203

80. Krause, F. and Raedler, K.H. (1980) Mean-Field Magnetohydrodynamics and Dynamo Theory.

81. Popova, H. and Sokoloff, D. (2008) Meridional Circulation and Dynamo Waves. *Astronomische Nachrichten*, **329**, 766. https://doi.org/10.1002/asna.200811028

82. Benevolenskaya, E.E. (1995) Double Magnetic Cycle of Solar Activity. *Solar Physics*, **161**, 1-8. https://doi.org/10.1007/BF00732080

83. Steinhilber, F., Beer, J. and Fröhlich, C. (2009) Total Solar Irradiance during the Holocene. *Geophysics Research Letters*, **36**, L19704. https://doi.org/10.1029/2009GL040142

84. Zharkova, V.V., Shepherd, S.J., Zharkov, S.I. and Popova, E. (2019) Retracted Article: Oscillations of the Baseline of Solar Magnetic Field and Solar Irradiance on a Millennial Timescale. *Scientific Reports*, **9**, 9197. https://doi.org/10.1038/s41598-019-45584-3

85. Zharkova, V. (2021) Millennial Oscillations of Solar Irradiance and Magnetic Field in 600-2600. In: Bevelacqua, J., Ed., *Solar System Planets and Exoplanets*, IntechOpen, London, 30 p. https://doi.org/10.5772/intechopen.96450

86. Lockwood, M., *et al.* (2020) Semi-Annual, Annual and Universal Time Variations in the Magnetosphere and in Geomagnetic Activity: 1. Geomagnetic Data. *Journal of Space Weather and Space Climate*, **10**, 23. https://doi.org/10.1051/swsc/2020023

87. Fairbridge, R.W. and Shirley, J.H. (1987) Prolonged Minima and the 179-yr Cycle of the Solar Inertial Motion. *Solar Physics*, **110**, 191-210. https://doi.org/10.1007/BF00148211

88. Nagovitsyn, Y., Obridko, V. and Kuleshova, A. I. (2015) The Upper Limit of Sunspot Activity as Observed over a Long Time Interval. *Solar Physics*, **290**, 1285-1294. https://doi.org/10.1007/s11207-015-0657-4

89. Scafetta, N. (2014) Discussion on the Spectral Coherence between Planetary, Solar and Climate Oscillations: A Reply to Some Critiques. *Astrophysics and Space Science*, **354**, 275-299.

https://doi.org/10.1007/s10509-014-2111-8

90. Bretagnon, P. and Francou, G. (1988) Planetary Theories in Rectangular and Spherical Variables: VSOP87 Solution. *Astronomy and Astrophysics*, **202**, 309.

91. Folkner, W.M., Williams, J.G., Boggs, D.H., Park, R.S. and Kuchynka, P. (2014) The Planetary and Lunar Ephemerides DE430 and DE431. Interplanetary Network Progress Report 42-196, 1-81.

92. Cionco, R.G. and Pavlov, D.A. (2018) Solar Barycentric Dynamics from a New Solar-Planetary Ephemeris. *Astronomy and Astrophysics*, **615**, A153. https://doi.org/10.1051/0004-6361/201732349

93. Perminov, A.S. and Kuznetsov, E.D. (2018) Orbital Evolution of the Sun-Jupiter-Saturn-Uranus-Neptune Four-Planet System on Long-Time Scales. *Solar System Research*, **52**, 241-259. https://doi.org/10.1134/S0038094618010070

94. Le Mouël, J.-L., Lopes, F. and Courtillot, V. (2017) Identification of Gleissberg Cycles and a Rising Trend in a 315-Year-Long Series of Sunspot Numbers. *Solar Physics*, **292**, 43. https://doi.org/10.1007/s11207-017-1067-6

95. Fiori, W. (2022) A Faunal Approach to Understanding Ice Core Data, Milankovitch Cycles, the AGT and Ice Ages. Academia.edu 23.

96. Lean, J., Beer, J. and Bradley, R. (1995) Reconstruction of Solar Irradiance since 1610: Implications for Climate Change. *Geophysics Research Letters*, **22**, 3195-3198. https://doi.org/10.1029/95GL03093

97. Krivova, N.A., Solanki, S.K. and Unruh, Y.C. (2011) Towards a Long-Term Record of Solar Total and Spectral Irradiance. *Journal of Atmospheric and Solar-Terrestrial Physics*, **73**, 223-234. https://doi.org/10.1016/j.jastp.2009.11.013

98. Milankovich, M. (1998) Canon of Insolation and the Ice-Age Problem. Zavod za Udzbenike i Nastavna Sredstva, 307-310.

99. Steel, D. (2013) Perihelion Precession, Polar Ice and Global Warming. *Journal of Cosmology*, **22**, 10106-10129.

100. Akasofu, S.-I. (2010) On the Recovery from the Little Ice Age. *Natural Science*, **2**, 1211-1224. https://doi.org/10.4236/ns.2010.211149

101. Charvatova, I. (1988) The Solar Motion and the Variability of Solar Activity. *Advances in Space Research*, **8**, 147-150. https://doi.org/10.1016/0273-1177(88)90184-6

102. Lee, I., Robert, B., Gibson, M.A., Wilson, R.S. and Thomas, S. (1995) Long-Term Total Solar Irradiance Variability during Sunspot Cycle 22. *Journal of Geophysics Research*, **100**, 1667-1676. https://doi.org/10.1029/94JA02897

103. Willson, R.C. and Hudson, H.S. (1991) The Sun's Luminosity over a Complete Solar Cycle. *Nature*, **351**, 42-44. https://doi.org/10.1038/351042a0

104. Lockwood, M. and Stamper, R. (1999) Long-Term Drift of the Coronal Source Magnetic Flux and the Total Solar Irradiance. *Geophysics Research Letters*, **26**, 2461-2464. https://doi.org/10.1029/1999GL900485

105. Fligge, M. and Solanki, S.K. (2000) The Solar Spectral Irradiance since 1700. *Geophysics Research Letters*, **27**, 2157-2160. https://doi.org/10.1029/2000GL000067

106. Foukal, P., Fröhlich, C., Spruit, H. and Wigley, T.M.L. (2006) Variations in Solar Luminosity and Their Effect on the Earth's Climate. *Nature*, **443**, 161-166. https://doi.org/10.1038/nature05072

107. Stauning, P. (2011) Solar Activity-Climate Relations: A Different Approach. *Journal of Atmospheric and Solar-Terrestrial Physics*, **73**, 1999-2012. https://doi.org/10.1016/j.jastp.2011.06.011

108. Lean, J. (2000) Evolution of the Sun's Spectral Irradiance since the Maunder Minimum. *Geophysics Research Letters*, **27**, 2425-2428. https://doi.org/10.1029/2000GL000043

109. Shindell, D.T., Schmidt, G.A., Mann, M.E., Rind, D. and Waple, A. (2001) Solar Forcing of Regional Climate

Change during the Maunder Minimum. *Science*, **294**, 2149-2152. https://doi.org/10.1126/science.1064363

110. Miller, G.H., *et al.* (2012) Abrupt Onset of the Little Ice Age Triggered by Volcanism and Sustained by Sea-Ice/Ocean Feedbacks. *Geophysics Research Letters*, **39**, L02708. https://doi.org/10.1029/2011GL050168

111. Easterbrook, D.J. (2016) Evidence-Based Climate Science. Elsevier, Amsterdam.

112. Archibald, D. (2022) Methane: Much Ado about Nothing. The Wentworth Report 5.

113. Held, I.M. (2013) Climate Science: The Cause of the Pause. *Nature*, **501**, 318-319. https://doi.org/10.1038/501318a

114. Kosaka, Y. and Xie, S.-P. (2013) Recent Global-Warming Hiatus Tied to Equatorial Pacific Surface Cooling. *Nature*, **501**, 403-407. https://doi.org/10.1038/nature12534

115. Alimonti, G., Mariani, L., Prodi, F. and Ricci, R.A. (2022) A Critical Assessment of Extreme Events Trends in Times of Global Warming. *European Physical Journal Plus*, **137**, 112. https://doi.org/10.1140/epjp/s13360-021-02243-9